

A deep kinematic survey of planetary nebulae in the Andromeda Galaxy using the Planetary Nebula Spectrograph

H. R. Merrett¹, M. R. Merrifield¹, N. G. Douglas², K. Kuijken^{3,2}, A. J. Romanowsky^{4,1}, N. R. Napolitano^{5,2}, M. Arnaboldi^{6,7}, M. Capaccioli⁸, K. C. Freeman⁹, O. Gerhard¹⁰, L. Coccato², D. Carter¹¹, N. W. Evans¹², M. I. Wilkinson¹², C. Halliday¹³, T. J. Bridges¹⁴

¹*School of Physics and Astronomy, The University of Nottingham, NG7 2RD, UK*

²*Kapteyn Astronomical Institute, PO Box 800, NL-9700 AV Groningen, The Netherlands*

³*Leiden Observatory, PO Box 9513, NL-2300 RA Leiden, The Netherlands*

⁴*Departamento de Física, Universidad de Concepción, Casilla 160-C, Concepción, Chile*

⁵*INAF, Osservatorio di Capodimonte, Via Moiariello 16, Naples 80131, Italy*

⁶*ESO, Karl-Schwarzschild Str. 2, 85748 Garching bei Munchen, Germany*

⁷*INAF, Osservatorio Astronomico di Torino, Strada Osservatorio 20, I-10025 Pino Torinese, Italy*

⁸*Department of Physical Sciences, University of Naples Federico II, via Cinthia, 80126 Napoli, Italy*

⁹*Research School of Astronomy and Astrophysics, Australian National University, Canberra ACT 2601, Australia*

¹⁰*Astronomisches Institut, Universität Basel, Venusstrasse 7, CH 4102 Binningen, Switzerland*

¹¹*Astrophysics Research Institute, Liverpool John Moores University, Twelve Quays House, Egerton Wharf, Birkenhead CH41 1LD, UK*

¹²*Institute of Astronomy, Madingley Road, Cambridge CB3 0HA, UK*

¹³*INAF, Osservatorio Astrofisico di Arcetri, Largo E. Fermi 5, I-50125, Firenze, Italy*

¹⁴*Department of Physics, Queen's University, Kingston, Ontario, K7L 3N6, Canada*

Accepted 2006 ??????. Received 2006 ?????? ??; in original form 2006 January ??

ABSTRACT

We present a catalogue of positions, magnitudes and velocities for 3300 emission-line objects found by the Planetary Nebula Spectrograph in a survey of the Andromeda Galaxy, M31. Of these objects, 2615 are found likely to be planetary nebulae (PNe) associated with M31. The survey area covers the whole of M31's disk out to a radius of 1.5° . Beyond this radius, observations have been made along the major and minor axes, and the Northern Spur and Southern Stream regions. The calibrated data have been checked for internal consistency and compared with other catalogues. With the exception of the very central, high surface brightness region of M31, this survey is complete to a magnitude limit of $m_{5007} \sim 23.75$, 3.5 magnitudes into the planetary nebula luminosity function.

We have identified emission-line objects associated with M31's satellites and other background galaxies. We have examined the data from the region tentatively identified as a new satellite galaxy, Andromeda VIII, comparing it to data in the other quadrants of the galaxy. We find that the PNe in this region have velocities that appear to be consistent with membership of M31 itself.

The luminosity function of the surveyed PNe is well matched to the usual smooth monotonic function. The only significant spatial variation in the luminosity function occurs in the vicinity of M31's molecular ring, where the luminosities of PNe on the near side of the galaxy are systematically ~ 0.2 magnitudes fainter than those on the far side. This difference can be explained naturally by a modest amount of obscuration by the ring. The absence of any difference in luminosity function between bulge and disk suggests that the sample of PNe is not strongly populated by objects whose progenitors are more massive stars. This conclusion is reinforced by the excellent agreement between the number counts of PNe and the R-band light.

The number counts of kinematically-selected PNe also allow us to probe the stellar distribution in M31 down to very faint limits. There is no indication of a cut-off in M31's disk out to beyond four scale-lengths, and no signs of a spheroidal halo population in excess of the bulge out to 10 effective bulge radii.

We have also carried out a preliminary analysis of the kinematics of the surveyed PNe. The mean streaming velocity of the M31 disk PNe is found to show a significant asymmetric drift out to large radii. Their velocity dispersion, although initially declining with radius, flattens out to a constant value in the outer parts of the galaxy. There are no indications that the disk velocity dispersion varies with PN luminosity, once again implying that the progenitors of PNe of all magnitudes form a relatively homogeneous old population. The dispersion profile and asymmetric drift results are shown to be mutually consistent, but require that the disk flares with radius if the shape of its velocity ellipsoid remains invariant.

Key words: Local Group – galaxies: individual: M31 – galaxies: kinematics and dynamics –

arXiv:astro-ph/0603125v2 13 Mar 2006

1 INTRODUCTION

Observations of the distribution of stellar velocities in the solar neighbourhood of the Milky Way reveal a wealth of complex structure (Dehnen & Binney 1998). For a dynamical entity such as the Galaxy, this structure is as fundamental as the spatial arrangement of its stars, and should contain a mass of information as to the system's current state, as well as archaeological clues as to how it formed. Unfortunately, such data from a single locality are difficult to interpret in terms of the global structure of the galaxy. Although kinematic observations of more distant stars in the Milky Way have been made (see, for example, Sevenster et al. 1997), the complexity of disentangling the geometry of our own galaxy make such data difficult to interpret. We also clearly need more than one example before any general conclusions about the dynamics of disk galaxies can be drawn. An obvious next target is therefore the Milky Way's nearby sister system, the Andromeda Galaxy, M31.

However, studying the detailed kinematics of stars in even a nearby external galaxy is quite challenging. In fact, the first problem arises from its very nearness: M31 subtends such a large angle on the sky that many spectroscopic instruments are unable to survey the whole system within a realistic time. Further, even at what by extragalactic standards is the very modest distance of 785 ± 25 kpc (McConnachie et al. 2005), obtaining high-quality spectra of individual stars is challenging; it is only relatively recently that the requisite observations of even bright red giant branch (RGB) stars have been made (Reitzel & Guhathakurta 2002; Ibata et al. 2004; Kalirai et al. 2005).

Planetary nebulae (PNe) have long been recognised as a potentially simpler dynamical tracer of the stellar population. Stars evolve very rapidly but quite gently from the RGB phase to become PNe, so the kinematics of these two populations should be essentially identical. Further, the presence of strong emission lines in PNe make them quite easy to identify, and render the measurement of their Doppler shifts fairly trivial. More than twenty years ago, Nolthenius & Ford (1984) reported on kinematic measurements of 34 PNe in M31, but it was not until recently with the development of wide-field multi-object spectrographs that it has become possible to start to obtain the large sample necessary for dynamical studies (Hurley-Keller et al. 2004; Halliday et al. 2006). Even with such instruments, these studies involve both narrow-band imaging to identify candidate PNe and subsequent spectral follow-up, and this complex two-stage process has limited astronomers' enthusiasm for such projects. However, the recently-commissioned Planetary Nebula Spectrograph has reduced this process to a single stage, simultaneously identifying PNe and measuring their velocities. We have therefore used this instrument to carry out a deep kinematic survey of PNe over ~ 6 square degrees, covering the bulk of M31's visible area.

This paper describes the survey, tabulates the final data set of 3300 detected emission-line objects (of which 2730 are probably PNe, 2615 in M31), and presents some initial analysis of these data. In Section 2, we briefly describe the instrument and the observations made. A detailed description of the data analysis is presented in Section 3. Section 4 compares the photometric and kinematic results with those from previous smaller surveys, while Section 5 explores the contamination of the data by objects other than PNe and the sample's completeness. The catalogue resulting from all this analysis is presented in Section 6. In Section 7, we identify PNe associated with M31's satellites and other galaxies in the field, both to study these systems and to create a "clean" M31 sample. We end the paper with a preliminary analysis of the resulting sample of

M31 PNe: Section 8 investigates their luminosity function; Section 9 compares their spatial distribution with that of the starlight in the galaxy; Section 10 calculates the luminosity specific number density of PNe; and Section 11 examines the basic kinematic properties of M31's disk out to large radii that can be gleaned from these data. We draw conclusions and look to the future in Section 12.

2 INSTRUMENTATION AND OBSERVATIONS

2.1 The Planetary Nebula Spectrograph

The Planetary Nebula Spectrograph (PN.S), described in detail in Douglas et al. (2002), was designed specifically to measure the shifted wavelength (and hence velocity) of the 5007 \AA [O III] emission line that dominates the spectra of PNe. It makes this measurement using a technique called "counter-dispersed imaging." Light from the galaxy initially passes through a narrow-band filter ($\sim 35 \text{ \AA}$ wide) centred on the emission line. The light is then divided into two beams, with each beam dispersed by a grating before being imaged onto separate CCDs, termed the left- and right-arm images. As illustrated in Figure 1, we thus obtain a pair of slitless spectrographic images in which stellar continua appear as elongated streaks, or "star trails", and PNe are visible as dots from their [O III] emission lines. However, the two gratings are arranged to disperse the light in opposite directions, so the dots are offset from the true location of the PN in opposite directions as well. Thus, in essence, the mean location of the dots in the two images gives the position of a PN, while their separation yields its velocity.

The instrument's ability to obtain all the necessary information from a single observation, combined with its relatively large field of view,¹ make it a very efficient tool for studying PN kinematics in external galaxies. Its main drawback relative to the conventional approach of optical identification and follow-up spectroscopy is that the attainable velocity accuracy is somewhat lower at $\sim 15\text{--}20 \text{ km s}^{-1}$, compared with the $\sim 2\text{--}10 \text{ km s}^{-1}$ obtained from traditional spectroscopy (Halliday et al. 2006; Hurley-Keller et al. 2004; Ciardullo et al. 2004). However, this level of accuracy is good enough to study even quite subtle kinematic properties of external galaxies.

2.2 Observations

The PN.S observations for this survey were carried out on the William Herschel Telescope (WHT) in La Palma on two runs: 2002 October 8 – 13 and 2003 September 29 – October 5. In M31's halo, where PNe are scarce, supplementary imaging was used to optimise the choice of fields to be observed with PN.S. This imaging was obtained using the Wide Field Camera on the Isaac Newton Telescope (INT), also in La Palma, on 2003 August 16 – 21. Figure 2 shows the locations of the fields observed with both instruments.

Fifteen minute exposures were used for the majority of PN.S fields, although multiple observations were made for a few fields. INT WFC exposures were twenty minutes long through the narrow-band [O III] filter and two minutes with the off-band g' filter. For the PN.S observations, we used the instrument's 'A' filter at a 0°

¹ Mounted on the William Herschel Telescope using the Isaac Newton Group's EEV CCDs, the PN.S has a field of $10'39$ by $11'35$, with pixel scales of $0'301$ per pixel in the dispersed direction and $0'272$ per pixel in the non-dispersed direction, and a spectral dispersion of 0.775 \AA per $13.5 \mu\text{m}$ pixel.

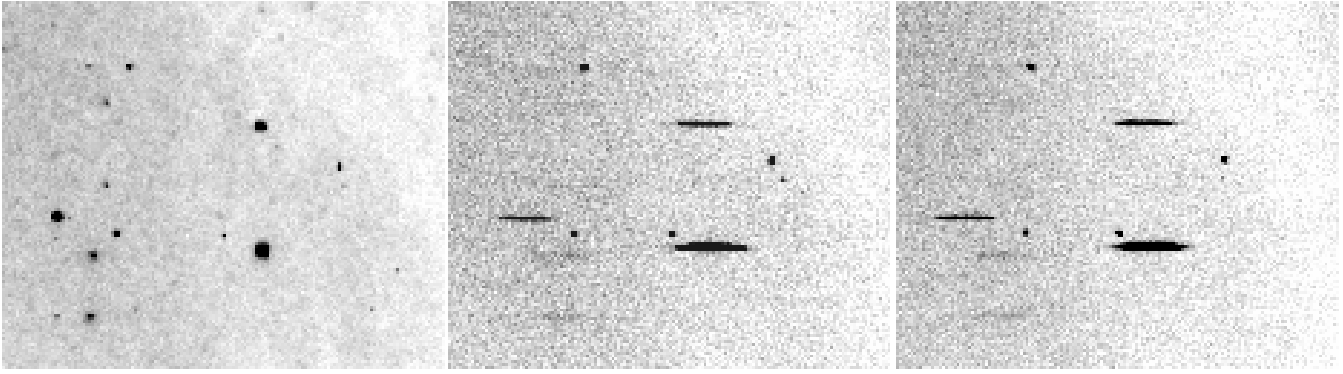


Figure 1. A sample of PN.S data. The left hand panel shows a conventional [O III] image of a small section of M31 (Massey et al. 2002), while the two right-hand panels show the same field as seen through the two arms of PN.S. Note how continuum objects are dispersed into “star trails” while [O III] emission-line objects remain as shifted point sources.

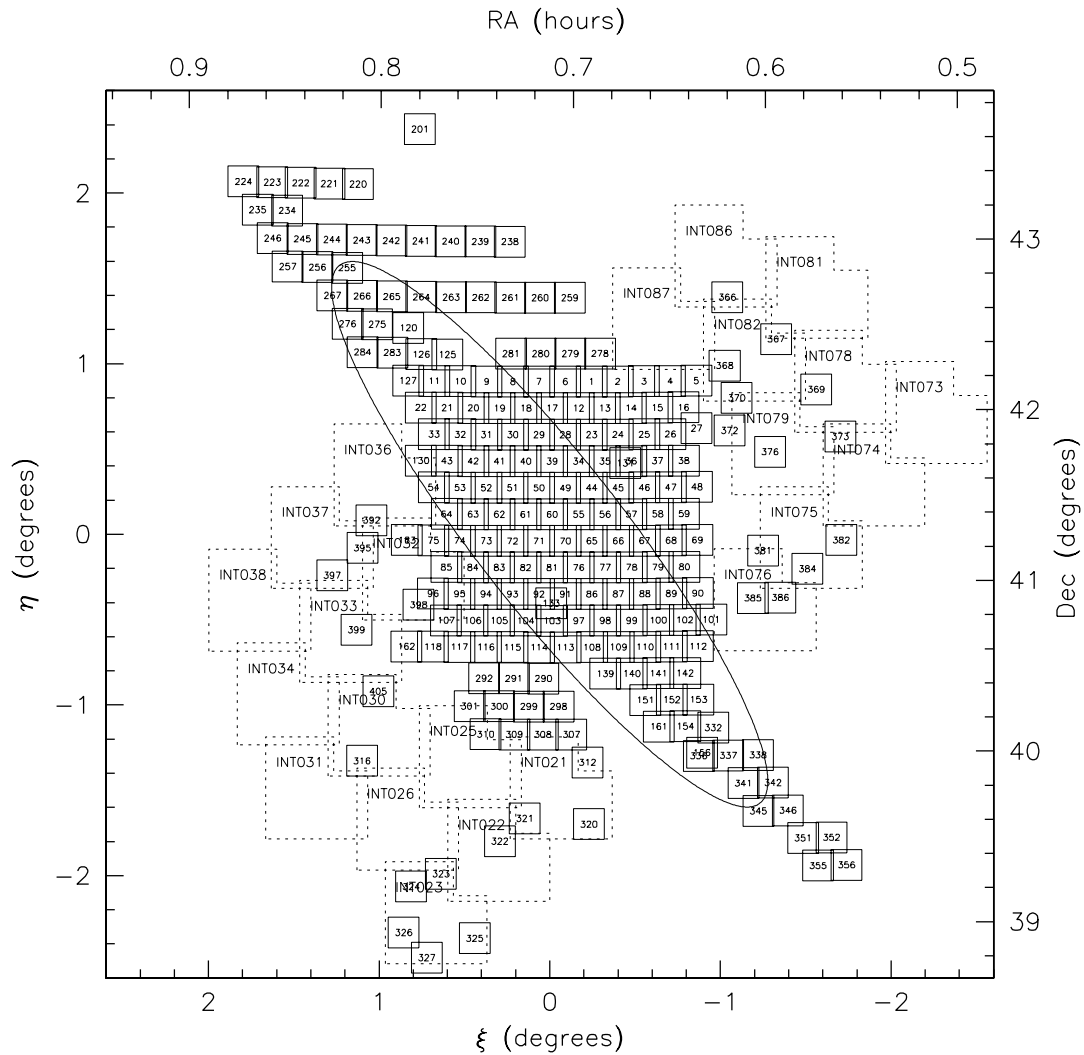


Figure 2. Fields observed in M31. The small square fields are PN.S field locations, with numbers 1-163 observed on the first PN.S run, the rest on the second; the larger fields with dotted outlines are the INT WFC fields. The ellipse marks a 2° (27.4 kpc) disk radius.

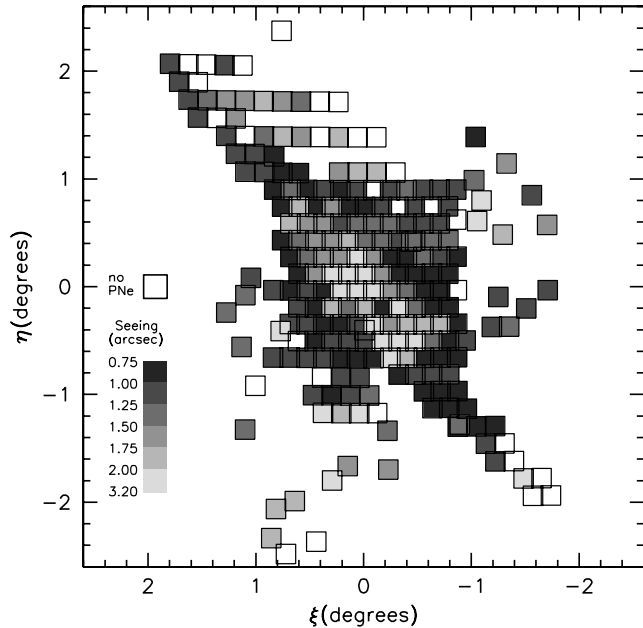


Figure 3. Seeing as measured for different survey fields. Darker squares represent better seeing, with values in arcseconds as given on the accompanying scale. Empty squares contained no detected PNe.

tilt angle (Douglas et al. 2002). This configuration provides a central wavelength of 5002.2 Å and a 36.5 Å bandwidth, allowing PNe to be detected with velocities between -1369 km s^{-1} and 817 km s^{-1} . This range is well matched to the velocity range of components of M31, which lie between $\sim -600 \text{ km s}^{-1}$ and 0 km s^{-1} , but also allows a significant margin for the detection of any unexpected high-velocity features.

The adopted survey strategy was to tile the entire area of M31’s disk out to a 2 degree radius with overlapped PN.S pointings. We also fully mapped regions of particular interest at larger radii, such as the Northern Spur and Southern Stream (Ibata et al. 2001). However, at larger radii PNe become sufficiently scarce that most fields would be completely empty, so we used the INT narrow-band imaging to identify candidate PNe, and only made PN.S observations of fields where at least one object had been detected. In total, 226 PN.S fields were observed.

Weather conditions varied considerably during the PN.S runs with two half nights lost to cloud cover during the first run, and four nights lost in the second. The seeing also changed significantly over the runs, with values between $0''.8$ and $3''.1$ recorded. To make optimum use of these varying conditions, we observed the central fields in the worst seeing conditions (see Figure 3): PNe are sufficiently plentiful in these fields that we did not need to get so far down the luminosity function to obtain a useful dynamical sample, and the high continuum surface-brightness in this region meant that we would in any case not be able to achieve completeness at fainter magnitudes (see Section 5). Confusion with discrete objects is not a significant problem in surveys of this type as stars must be fairly bright to leave a visible trail. Even the very brightest stars at the distance of M31 only leave faint stellar trails and in the bright central regions they are not visible above the background light.

3 DATA ANALYSIS

3.1 Wide Field Camera data reduction

The INT Wide Field Camera data frames were debiased and flat-fielded using standard data reduction packages in *IRAF*. The g' -band images were remapped to match the coordinates of the [O III] images, and *SExtractor* (Bertin & Arnouts 1996) was used in double-image mode to find sources in the [O III] image and simultaneously measure the flux of counterparts in the g' band. Objects with more than five times as many [O III] counts as g' counts were selected as potential PNe candidates for PN.S follow-up. These candidates were then visually confirmed individually, and their approximate positions were calculated; more accurate astrometry was not required as the PN.S has a large field of view.

3.2 Planetary Nebula Spectrograph data reduction

Since the PN.S is such an unconventional instrument, we have had to produce a customised data reduction package to convert the raw data to a scientifically-usable form. This package has been constructed within *IRAF*, supplementing the standard tasks with *Fortran* and *PGPLOT* extensions. Given the non-standard nature of this procedure, we now describe the reduction package and its application to the M31 observations in some detail.

3.2.1 Initial pipeline

Images were first debiased by subtracting a surface function fit to the pre- and over-scan regions using the *IRAF* task *imsurfit*. There was very little structure in the bias of the EEV CCDs, so the function subtracted was close to flat.

To map out and remove bad regions on the CCDs, zero-exposure bias frames were used to create a map of pixels where charge transfer problems have occurred. Skyflats were employed to locate other low-sensitivity pixels (by comparing to a median smoothed version; pixels with greater than 9σ difference between the two were taken to be bad). These maps were then combined with a list of known bad pixel regions to make a mask which is fed to the standard *IRAF* routine *fixpix* to correct all the flats and science images.

Normalised pixel response maps were made by dividing flats by a median-filtered image (to remove spatial structures) then combining the flats using weights (to keep the noise Poissonian) and rejection (to eliminate cosmic ray events). The science and calibration images were flatfielded by dividing through by this response map.

The next step is to remove any residual cosmic rays: if they were left in through the next stages that remap pixels, then they would become smeared out, and could well mimic the point-spread function of a PN, so it is important to eliminate them at this stage. The cosmic rays were identified and removed using the Laplacian cosmic ray identification routine, *lacos_im* (van Dokkum 2001), with five iterations and a contrast limit between the cosmic rays and the underlying object of 1.2. This produces fairly clean images and any residual cosmic ray events are unlikely to be a problem as there would have to be a pair of residuals in the two images in locations such that they could be a PN.

The resulting cleaned science images still contain curvatures and rotations which must be eliminated in order to match up the left-right image pairs. The distortions involved are somewhat complicated for a slitless spectrograph like the PN.S, since they involve

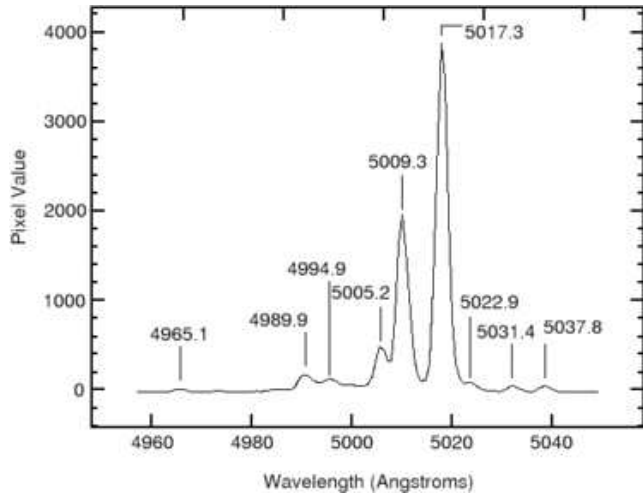


Figure 4. Detailed arc spectrum seen through filter-A set at 0° . The wavelengths of all the detected lines within the bandpass are annotated.

both imaging distortions and the wavelength calibration of the dispersed light. To determine the requisite mapping, we obtained frequent calibration images in which a mask containing 178 regularly-spaced holes is introduced into the beam (as described in detail in Douglas et al. 2002). By illuminating this mask with a copper-neon-argon arc lamp, we obtained an array of short filter-limited spectra on the CCD, allowing both the spatial mapping and the wavelength calibration of the instrument to be determined. As Figure 4 illustrates, even the small wavelength range admitted by the narrow-band filter contains a number of lines. We used the brightest of these lines (at 5017 \AA) to measure any departures in the locations of these dots from the regular array of holes in the mask, thus determining the spatial mapping. These distortions were then removed from the accompanying science images using *IRAF*'s standard geometrical mapping routines, *geomap* and *geotran*. Two other lines at 4990 \AA and 5009 \AA were then used in conjunction with the 5017 \AA line to characterise the wavelength calibration across the image by interpolating a quadratic solution between these points. A database of these solutions for the array of points on each CCD was produced; by interpolating between adjacent solutions, we can map directly from the locations of an object detected in the two arms, $\{x_L, y_L, x_R, y_R\}$ to a true position on the sky and an emission wavelength, $\{x_0, y_0, \lambda\}$.

Following the spatial correction step, it is also possible to co-add images in those cases where multiple observations of the same field have been taken. Any offsets between images were determined by measuring the positions of dispersed brighter stars in the field (selected from the USNO-B catalogue; Monet et al. 2003), and the necessary shifts were made. As a slight refinement, we actually performed both the image undistortion and this shift in a single transformation of the original image, so that there is only one interpolation of the data. We then combined the matched image frames using a weight determined by the quality of each image. These weights were calculated by using the *IRAF* routine *fitprofs* to fit a one-dimensional Gaussian across each star trail used in determining the shifts; the parameters of these fits were used to quantify the transparency, seeing and background level of each exposure. The appropriate weighting for each exposure was then given by

$$W = \frac{(\text{exposure time}) \times (\text{transparency})}{(\text{seeing})^2 \times (\text{background})}. \quad (1)$$

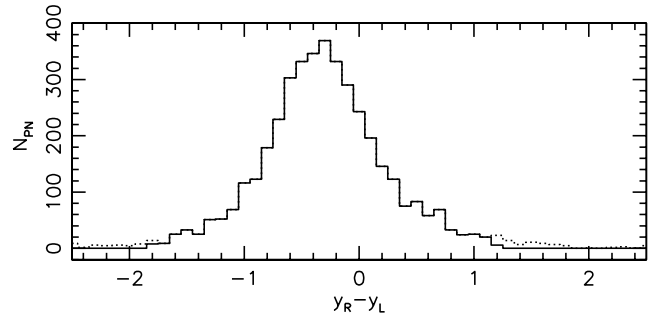


Figure 5. Difference in undispersed y coordinates of matched pairs of M31 point sources detected in the two arms of the PN.S. The dotted line shows those few pairs deemed spurious by the application of further cuts at $Y_R - Y_L = -1.80$ and 1.17 .

3.2.2 Identification of emission-line objects

Emission-line objects in the pipeline-processed images were identified by a semi-automated routine. The undistorted images from both left and right arm were median-subtracted to remove unresolved continuum from M31, and *SExtractor* was run on the image to detect point sources. In order to eliminate the incorrect identification of features in star trails as point sources, *SExtractor* was rerun on the same image after it had been convolved with an elliptical Gaussian function elongated in the dispersion direction; any sources originating from the stellar spectra were still found as this blurring has essentially no effect on star trails, so these false detections can be eliminated.

Sources independently identified from the two arms of the spectrograph were initially automatically matched in left–right pairs by selecting detections that have the same coordinate in the undispersed y directions to within two pixels, and whose coordinates in the dispersed x direction differ by an amount consistent with the bandpass of the filter and the wavelength calibration determined above. These candidate pairs were passed on to a custom-written *Fortran* routine which allows the two images to be examined side-by-side. Any false detections, such as confused points within extended structures, were eliminated at this point. Further manual inspection then added back in any detections that have been missed by the automated routine, usually due to proximity to the field edge or a star. The edited list of emission-line pairs was then passed to the *IRAF phot* routine to improve the position determination and to measure the brightness of the source [using an aperture radius equal to the mean full width at half maximum (FWHM) seeing for that field to minimise sky contamination]. The FWHM of each source was determined using the Moffat parameter returned by the *IRAF imexam* task, as this turned out to be the simplest robust metric.

Once the source positions on both arms have been refined in this way, we can apply a slightly more stringent cut in matching up the spatial coordinates of sources to eliminate chance alignments: as Figure 5 shows, the distribution of differences in the y coordinate between the two arms is significantly tighter than the initial cut of ± 2 pixels, so we deemed the objects in tails of the distribution to be chance alignments, and eliminated them from the source list.

At this point, we have the definitive list of pairs of objects, and by applying the calibration determined in Section 3.2.1 we can transform these coordinates into a spatial location and a wavelength. Identifying the emission with the 5007 \AA [O III] line, we can translate the observed wavelength into a velocity, which we correct to a heliocentric value on a field-by-field basis using *IRAF*'s *rvcorrect* routine. A measure of the internal consistency of these

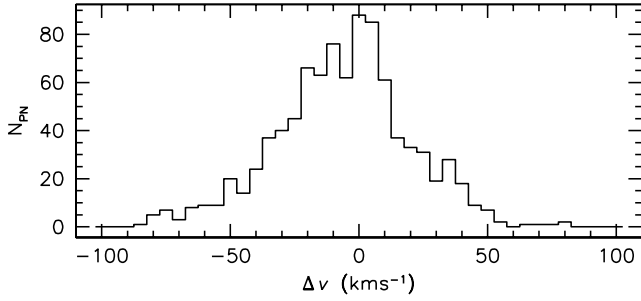


Figure 6. Differences between the velocities obtained for repeated observations of PNe in the overlaps between fields. A Gaussian fit gives a dispersion from P.N.S of 17 km s^{-1} .

velocities can be obtained using the PNe that lie in the overlaps between fields for which we have multiple velocity measurements. There are 732 objects detected in more than one field (643 in two fields, 88 in three fields, 1 in four fields), so we have quite a large sample to play with. Figure 6 shows the distribution of velocity differences between pairs of measurements. A Gaussian fit to these data gives a dispersion of 24 km s^{-1} , implying an error on each individual measurement of 17 km s^{-1} . This value is clearly an over-simplification since the distribution appears somewhat non-Gaussian and possibly even multi-modal. This complex shape can be attributed to the complexity involved in the wavelength calibration of slitless spectroscopy. However, the repeat observations used in Fig. 6 all lie close to the edges of the instrument’s field of view, where distortions in the wavelength solution are greatest and the amount of calibration data is smallest. The quoted error should therefore be viewed as conservative, but with some systematic residual errors on the scale of $\sim 5 - 10 \text{ km s}^{-1}$ not ruled out. Nonetheless, even these pessimistic errors are entirely adequate in a study of the large-scale kinematics of a massive galaxy like M31.

3.2.3 Astrometry

The measured coordinates must next be transformed into a standard reference frame. This process was carried out using the same basic routines used for image stacking (see Section 3.2.1). The approximate location of each field was determined from its nominal pointing, and star positions in the vicinity were read in from the USNO-B catalogue. The corresponding stars trails in the P.N.S images were found and locations calculated using *IRAF*’s *xregister* task; the resulting coordinates were fed to the *ccmap* task to calculate the astrometric solution for the field. In the very central fields, the bright background means there are very few stars available. In these fields, PN positions that have already been calibrated in overlapping neighbouring fields have been added to the list of coordinates, in order to bootstrap the astrometric solution across the central region.

The PNe in the overlap regions between fields also provide an internal check on the accuracy of the astrometry, by measuring offsets between the coordinates for the same source in different fields. As with the velocity consistency check described above, this will tend to be a conservative measure of accuracy, since spatial distortions are greatest near the edges of fields where overlaps exist, so one might expect the astrometric solution to be poorest in these regions. As Figure 7 shows, the astrometric accuracy is somewhat better in declination than right ascension. This difference arises because right ascension corresponds to the direction in which the calibrating stars are dispersed, so centroiding their emission in this di-

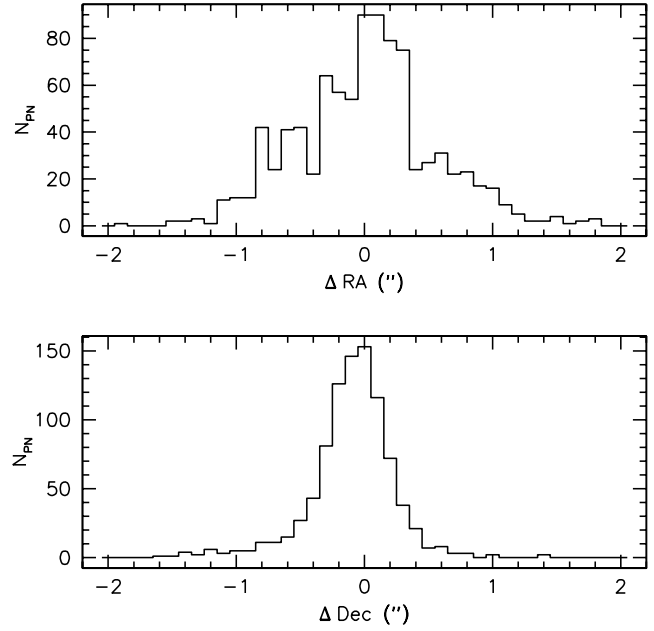


Figure 7. Differences between the positions obtained for repeated observations of PNe in the overlaps between fields. Gaussian fits to these give measurement uncertainties of $\sigma_{\text{RA}} = 0''.34$ and $\sigma_{\text{Dec}} = 0''.16$.

rection is fundamentally less accurate. However, the absolute positional accuracy is more than adequate for this large-scale kinematic survey of M31.

The astrometric matching of fields also allows us to make a final pass through the list of detected sources to eliminate the duplicate detections from field overlaps. Where the duplicate observations were obtained under similar seeing conditions, the positions, fluxes and velocities of the two detections were simply averaged; where the seeing conditions vary by more than $0''.5$, just the better-quality data were used.

For this survey, it is also useful to obtain the coordinates in an M31-based reference frame. We have therefore followed the geometric transformations of Huchra et al. (1991), which define right ascension and declination offsets relative to the centre of M31, $\{\xi, \eta\}$, and coordinates aligned with the system’s major and minor axes, $\{X, Y\}$, via the relations

$$\xi = \sin(\text{RA} - \text{RA}_0) \cos(\text{Dec}), \quad (2)$$

$$\eta = \sin(\text{Dec}) \cos(\text{Dec}_0) - \cos(\text{RA} - \text{RA}_0) \cos(\text{Dec}) \sin(\text{Dec}_0), \quad (3)$$

$$X = -\xi \sin(\text{PA}) - \eta \cos(\text{PA}), \quad (4)$$

$$Y = -\xi \cos(\text{PA}) + \eta \sin(\text{PA}). \quad (5)$$

here, we have taken the centre of M31 to lie at $\text{RA}_0 = 00^{\text{h}}42^{\text{m}}44^{\text{s}}.3$, $\text{Dec}_0 = 41^{\circ}16'09''$ (J2000.0), and have adopted a position angle for the major axis of $\text{PA} = 37^{\circ}.7$ (de Vaucouleurs 1958). With this choice of coordinates, positive X is located southwest of the centre of M31 and positive Y lies to the northwest.

3.2.4 Flux calibration

Although not primarily designed as a photometric instrument, the P.N.S does provide information on the magnitudes of detected PNe through the brightness of the spots in the two arms. However, the

Table 1. Instrumental efficiencies calculated from spectrophotometric standard stars.

Star	F_{5007} ($\text{erg s}^{-1} \text{\AA}^{-1}$)	Date	Efficiency		
			Left	Right	Total
LDS 749B ^a	154.759	2002-10-10	0.1424	0.1467	0.2891
BD+33 2642 ^b	6367.221	2002-10-10	0.1305	0.1322	0.2628
G193-74 ^c	63.438	2002-10-13	0.1533	0.1393	0.2926
BD+17 4708 ^c	18303.018	2003-09-29	0.1454	0.1435	0.2890
BD+28 4211 ^c	8708.624	2002-10-08	0.1365	0.1325	0.2691
BD+28 4211 ^c	8708.624	2002-10-10	0.1331	0.1290	0.2621
BD+28 4211 ^c	8708.624	2002-10-11	0.1328	0.1299	0.2626
BD+28 4211 ^c	8708.624	2002-10-11	0.1322	0.1312	0.2634
BD+28 4211 ^c	8708.624	2002-10-12	0.1331	0.1298	0.2629
BD+28 4211 ^c	8708.624	2003-09-29	0.1438	0.1414	0.2852
BD+28 4211 ^c	8708.624	2003-09-30	0.1371	0.1292	0.2662

References: ^a Oke (1974), ^b Oke & Gunn (1983), ^c Oke (1990)

Table 2. Extinction per unit airmass in r' from the Carlsberg Meridian Telescope, and weather notes for the nights observed.

Night	Ext, r'	Error	Ext ₅₀₀₀ ^a	Error	Comments
2002-10-08	0.101	0.004	0.172	0.007	Rain at end
2002-10-09	0.129:	0.029	0.219:	0.049	Cloud first half
2002-10-10	0.106	0.006	0.180	0.010	
2002-10-11	0.107	0.005	0.182	0.009	
2002-10-12	0.106	0.005	0.180	0.009	
2002-10-13	0.112	0.009	0.190	0.015	
2003-09-29	0.234:	0.024	0.398:	0.041	
2003-09-30	0.213:	0.012	0.362:	0.020	Cloudy at start
2003-10-01	0.317:	0.068	0.539:	0.116	Mostly cloudy
2003-10-02	-	-	-	-	Mostly rain
2003-10-03	-	-	-	-	Rain and cloud
2003-10-04	-	-	-	-	Rain
2003-10-05	-	-	-	-	Rain

^a The conversion to Ext₅₀₀₀ is calculated from Table 1 in RGO/La Palma Technical Note 31 to be a factor 1.70. 5000 Å is the closest listed value to the filter central wavelength.

conversion of count rates into fluxes is not entirely straightforward. The PN.S has a rather slow shutter that takes some 15 seconds to fully open or close, so the effective vignetting in short exposures is significantly different from that in long exposures. This limitation means that we could not use sky flats to determine the overall vignetting, so instead used long exposure dome flats obtained during the day. To obtain an optimal vignetting function, dome flats obtained at many position angles were averaged to render the illumination of the field as uniform as possible. Since our science exposures are 15 minutes long, we have not applied any correction for the small variation in effective exposure time due to the slow shutter.

We measured the total system efficiency for PN.S in the observational setup described using observations of spectrophotometric standard stars. The flux per unit wavelength was measured from a narrow column through the brightest region of the stellar trail and compared with the published value. As Table 1 shows, the total system efficiency estimates are found to be surprisingly consistent, with a mean value of $\text{Eff}_{\text{total}} = 27.3 \pm 0.4\%$, with much of the scatter attributable to the non-photometric conditions. As only a few standard stars observations were made during the run this level

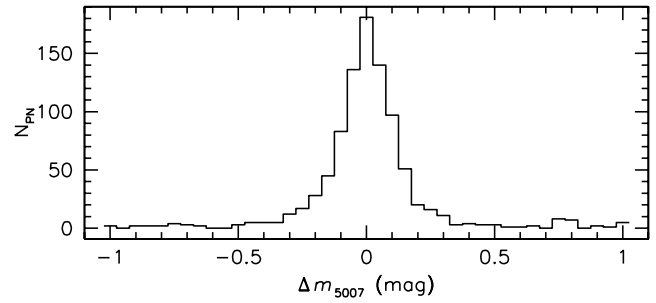


Figure 8. Magnitude variations within the PN.S data set from PNe in field overlaps. A Gaussian fit to this gives a measurement uncertainty of $\sigma_{m_{5007}} = 0.07$ mag.

of consistency may be artificially low. However, since the science goals of this kinematic survey do not require high precision photometry, this uncertainty is of little significance.

Fluxes of the detected sources were then calibrated using the formula

$$F_{5007} = \frac{(C_L \cdot g_L + C_R \cdot g_R) E_{5007}}{\text{Eff}_{\text{total}}} A T_{\text{exp}} 10^{\left(\frac{a_{\text{sky}} a_{\text{Gal}}}{2.5}\right)}, \quad (6)$$

where C_L and C_R are the total counts from the left and right arms; g_L and g_R are the gains of the CCDs on each arm; E_{5007} is the energy of a photon at 5007 Å; A is the effective geometric collecting area of the telescope and is equal to 13.85 m²; T_{exp} is the exposure time; a_{sky} is the nightly sky extinction as recorded by the Carlsberg Meridian Telescope (see Table 2) multiplied by the airmass at which the field was observed; and a_{Gal} the Galactic extinction taken from Schlegel et al. (1998) and corrected to our filter central wavelength using the relation from Cardelli et al. (1989) giving a value of $a_{\text{Gal}} = 0.226$. The conversion to PN-specific magnitudes follows the Jacoby (1989) relationship,

$$m_{5007} = -2.5 \log(F_{5007}) - 13.74, \quad (7)$$

where the zero-point is chosen such that an emission line object would have the same apparent magnitude as would be recorded if observed through a V-band filter. To give a sense of this zero-point for objects in our catalogue, the resulting magnitudes range from a fairly bright H II region at 17.8 mag to the faintest PNe at ~ 26 mag.

Once again, we can obtain an internal estimate of the uncertainty in magnitudes by comparing the values derived for duplicate observations in the overlaps between fields. Figure 8 shows the differences between magnitudes in these repeated observations; a Gaussian fit to this distribution gives a rather small measurement uncertainty of $\sigma_{m_{5007}} = 0.07$ mag. Magnitudes for extended objects will be systematically underestimated by this technique as no allowance has been made in the choice of aperture size for objects that are larger than the field point-spread function. However, since the main focus of this survey is to determine the properties of unresolved PNe, this issue is also not a major concern.

4 COMPARISON WITH OTHER DATA SETS

One concern with any data set from a novel instrument like the PN.S is that it may contain unpredicted systematic errors. Fortunately, a number of smaller data sets obtained using more conventional instrumentation already exist, so we can compare the new data with these subsets to check for such systematic effects.

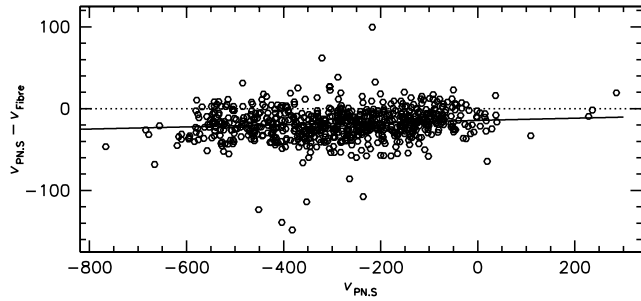


Figure 9. Comparison of initial PN.S velocities to Halliday et al. (2006) fibre-spectrograph velocities. The solid line shows a fit to the data, while the dotted line is at 0 km s^{-1} .

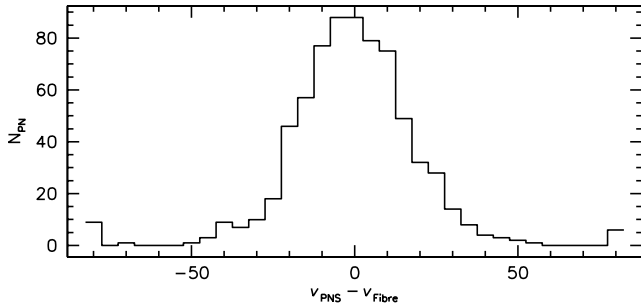


Figure 10. Plot of the difference between final PN.S velocities and Halliday et al. (2006) fibre-spectrograph velocities. A Gaussian fit gives $\Delta v = -0.7 \pm 0.4 \text{ km s}^{-1}$ and $\sigma = 15.4 \pm 0.4 \text{ km s}^{-1}$.

4.1 Velocity comparison

The largest existing kinematic survey of PNe in M31 is that by Halliday et al. (2006, hereafter H06), which determined velocities for 723 PNe using the conventional approach of narrow-band imaging and fibre-fed spectroscopy. Of these PNe, we find 715 objects within $4''$ of a PN.S object; the remaining 8 are likely obscured behind stellar trails in the PN.S images, but a 99% recovery rate is very respectable, and already gives a measure of the completeness for these brighter PNe.

If we plot the difference between H06 and PN.S velocities against the PN.S velocity, as in Figure 9, we find a small zero-point offset and a very slight linear dependence on velocity, fitted by the relation

$$v_{\text{PN.S}} - v_{\text{H06}} = 0.0151v_{\text{PN.S}} - 17.0. \quad (8)$$

This small systematic effect presumably arises from the limitations of the restricted range of arc lines available for PN.S wavelength calibration (see Figure 4). There is no large scale spatial dependence in this velocity difference, though there appears to be some small variation within the PN.S field. It makes very little difference to any of the scientific results, but for consistency we have applied the correction implicit in equation (8) to our complete data set and for all subsequent analysis. The residual differences in velocity between PN.S and H06 data are shown in Figure 10. Fitting a Gaussian to this distribution gives a dispersion of 15.4 km s^{-1} ; H06 quote an error of 6 km s^{-1} for their fibre spectroscopy, implying that the PN.S data have an uncertainty of 14 km s^{-1} . This value is somewhat smaller than the error deduced from self-calibration for the reasons discussed above, and is probably a more accurate measure of the true uncertainty in the PN.S velocities.

An estimate of M31's system velocity for the PN.S data was

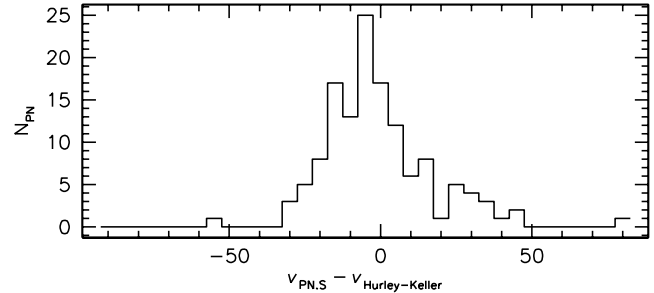


Figure 12. Plot of the difference between the final PN.S and the Hurley-Keller et al. (2004) velocities. A Gaussian fit gives $\Delta v = -5 \pm 1 \text{ km s}^{-1}$ and $\sigma = 12 \pm 1 \text{ km s}^{-1}$.

made by averaging the mean velocities from radial bins on either side of the major axis for data within 1° (~ 2.3 scale lengths) of the centre so as to exclude warps and asymmetries that have been observed at large radial distances, leading to a value of -309 km s^{-1} . This measurement is in reasonable agreement with the standard value of $-300 \pm 4 \text{ km s}^{-1}$ (de Vaucouleurs et al. 1991) and in good agreement with H06's value of -309 km s^{-1} .

As a test of the robustness of this velocity cross-calibration, we can also compare our results with a smaller but differently located survey carried out by Hurley-Keller et al. (2004). They surveyed one quadrant of M31's halo, finding a total of 146 emission-line objects, 135 PNe associated with M31, eight in M32 and three H II regions in Andromeda IV (see Figure 11). We have covered the majority of their survey area, finding 126 of their emission-line objects. The distribution of differences in velocities is shown in Figure 12. A Gaussian fit to this distribution gives a mean velocity difference of $-5 \pm 1 \text{ km s}^{-1}$ and a combined dispersion of 12 km s^{-1} , lower than the claimed PN.S velocity error. However, the distribution of errors here is clearly non-Gaussian, so not too much weight should be given to the exact value. Nonetheless, the errors are clearly small, well below a level that would compromise this kinematic study of M31.

4.2 Astrometric comparison

The PN.S astrometry can also be compared with the H06 data set. The distribution of differences in coordinates are shown in Figure 13. The right ascension distribution is similar to that found internally within the PN.S data, with a combined dispersion of $\sim 0''.6$. In declination there is a small systematic offset of $+0''.18$, with a long tail to positive values. As Figure 13 shows, the tails of the distribution are almost entirely populated by PNe from the four central PN.S fields. As discussed above, the lack of measurable stars in these fields compromises the PN.S astrometric solution somewhat, so such larger errors are not surprising. Excluding these fields, the combined dispersion in declination is $\sim 0''.2$. Given the enormous size of M31, such uncertainties are completely negligible for kinematic purposes.

4.3 Photometric comparison

Although not principally a photometric survey, we have been able to obtain fairly consistent magnitudes from the PN.S data, so once again it would be useful to compare against other data to obtain an external measure of the data quality. Fortunately, M31 has been extensively imaged as part of the Local Group Survey (Massey et al.

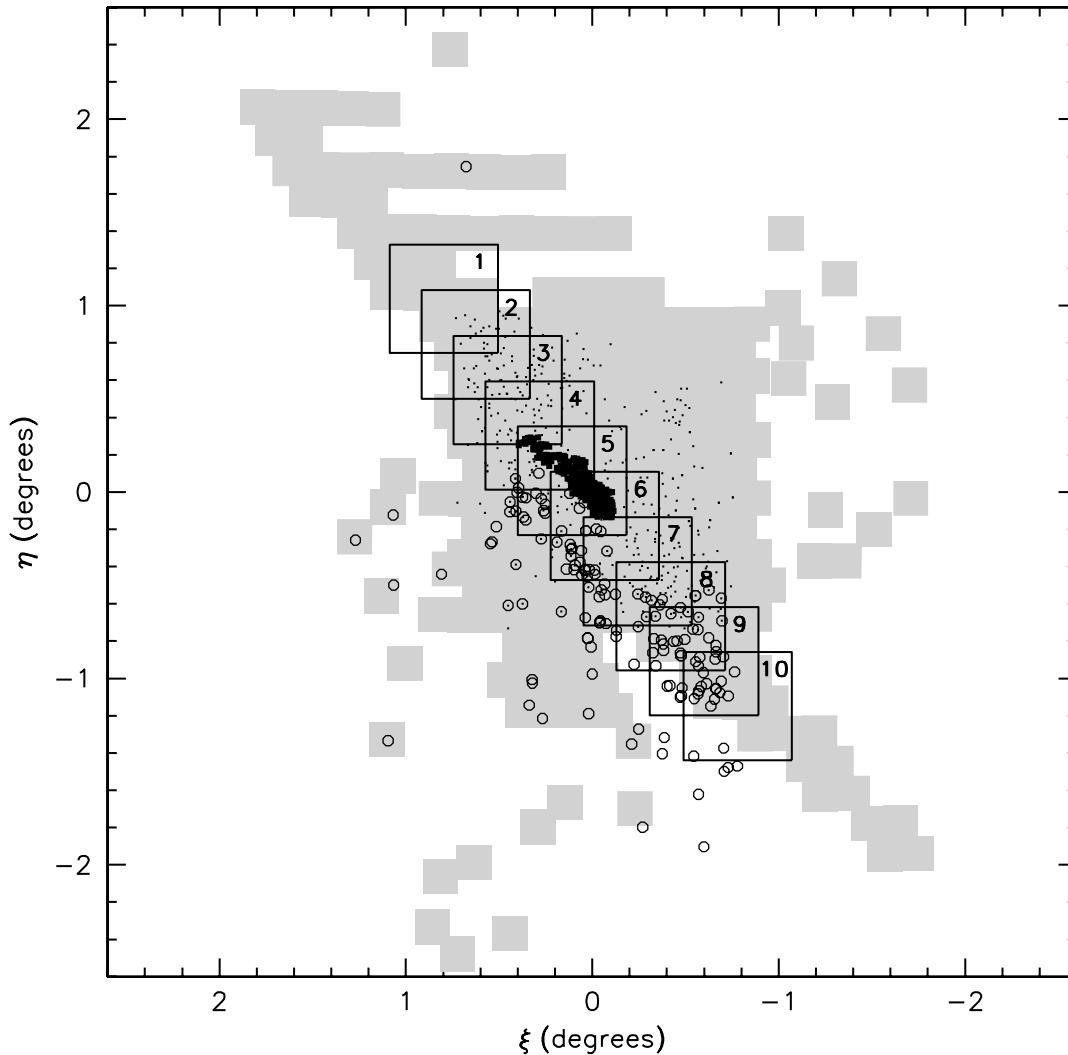


Figure 11. Positions of other surveys with respect to the PN.S survey. The PN.S survey area is shown in grey; Local Group Survey fields (Massey et al. 2002) are the large fields with solid outlines; the Ciardullo et al. (1989) data are the solid black points near the centre; the open circles are the Hurley-Keller et al. (2004) data; and the small points are H06's fibre spectroscopy data.

2002, hereafter M02), which includes narrow band studies of both the [O III] line and $H\alpha + [N II]$ lines. As Figure 11 shows, M02 imaged 10 fields over the majority of the disk of M31 and hence a large portion of the PN.S survey region (covering 2745 of the objects in the PN.S survey).

We therefore analysed the M02 survey images by obtaining fluxes at the positions of PN.S sources using the *IRAF phot* task with a fixed aperture of $2''$ – a value somewhat larger than the typical survey seeing ($\sim 0''.8 - 1''.5$) to allow for positional uncertainties, but not so large as to introduce significant source confusion. The photon counts were converted to fluxes using factors of 3.92×10^{-16} and 1.79×10^{-16} for the [O III] and $H\alpha + [N II]$ data respectively (Massey, private communication). Galactic extinction corrections were made using data from Schlegel et al. (1998) and Cardelli et al. (1989), as for the PN.S data, yielding extinctions of 0.225 mag and 0.164 mag for [O III] and $H\alpha + [N II]$ respectively.

Figure 14 shows the comparison between the imaging magnitudes derived in this way and the PN.S data. If we remove the faintest PNe for which photometry is rather uncertain, and probable H II regions for which this aperture photometry is inappropri-

ate, there is a good overall agreement between the data sets. Fitting a Gaussian to the remaining 1769 PNe gives negligible zero-point offset of 0.02 mag, and a combined dispersion of 0.16 mag. There is no evidence for varying offsets in different fields or for data taken on different nights.

As a further cross-check, Figure 15 shows the comparison between the PN.S magnitudes and the smaller data set published by Ciardullo et al. (1989). As expected, the scatter increases somewhat for the fainter PNe, but the overall agreement is very good. A Gaussian fit to the magnitude differences yields a mean of 0.00 mag with a combined dispersion of 0.13 mag, and even at the faintest magnitude the combined dispersion is less than 0.3 mag. Once again, there is no evidence of varying offsets for different fields or data taken on different nights. Since we are only going to use the photometric data to make quite crude cuts in the luminosity function of PNe, which we have measured over a range of more than three magnitudes, photometry with an error of less than 0.3 magnitudes is all that is required.

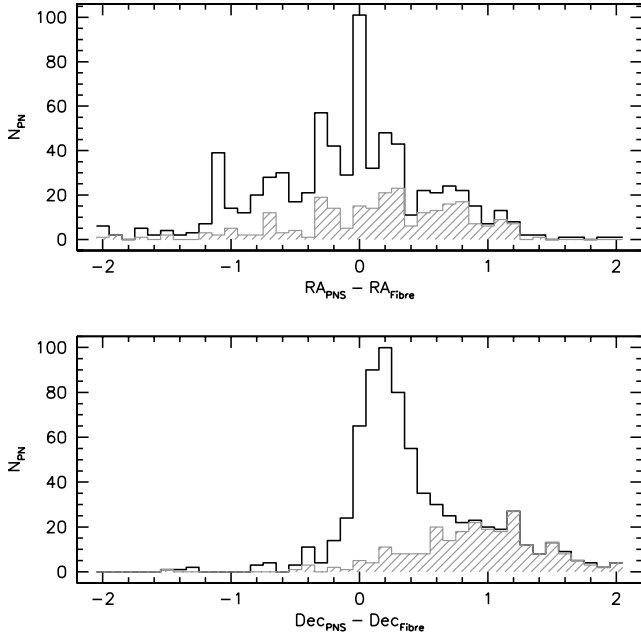


Figure 13. Comparison between PN.S and H06 astrometry, with differences measured in arcseconds. The black line represents all the PNe found in both catalogues; the grey shaded area shows those PNe in the central PN.S fields (60, 61, 70, 71)

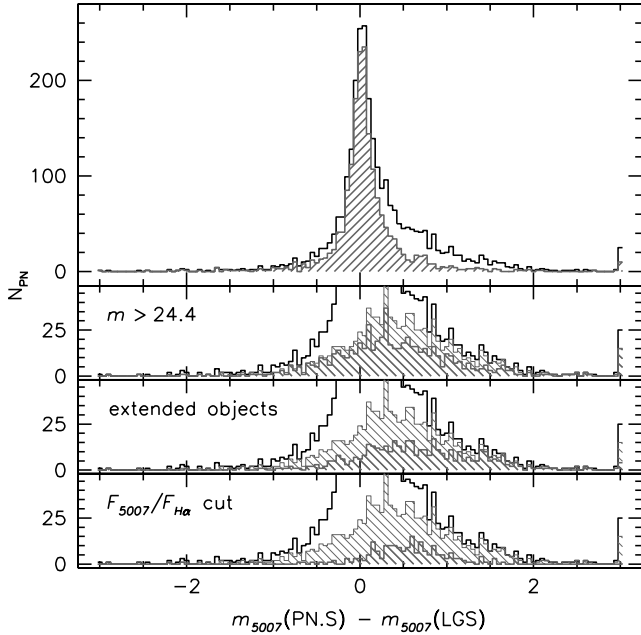


Figure 14. Photometric comparison between the magnitudes derived from the PN.S data and those from the Massey et al. (2002) imaging data. The black outline represents all the objects that are within both surveys. In the upper panel the shaded area represents PN remaining after a number of cuts have been applied to the data. The lower panels show the distribution of objects for the cuts indicated. The larger, light grey area is the total cut made while the smaller dark grey histograms show the particular objects being excluded by each criterion.

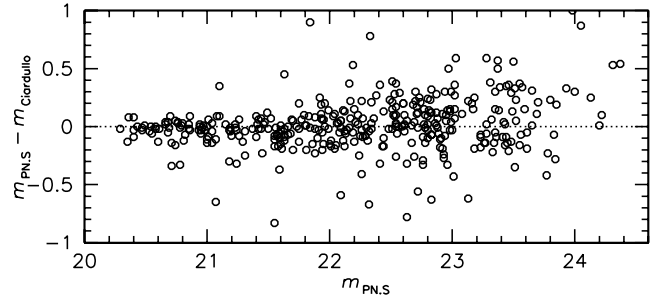


Figure 15. Comparison between PN.S magnitudes and those published in Ciardullo et al. (1989). Examining this plot by eye there appears to be a slight trend, with PN.S magnitudes being fainter than the corresponding Ciardullo et al. (1989) magnitudes for faint PNe. However, gaussian fits in half magnitude bins show this to be small (< 0.1 mag) and of low significance.

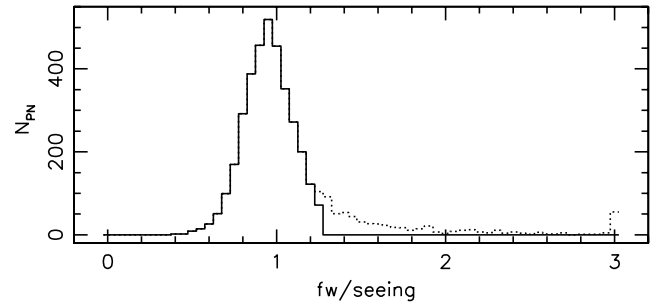


Figure 16. A plot of the FWHM of sources detected by the PN.S survey, normalised by the seeing of each observed field. Sources in the dotted long tail toward large sizes have been flagged as contaminating H II regions. The cut between extended and point sources is made at $fw/seeing = 1.25$.

5 CONTAMINATION AND COMPLETENESS

The next issue to be addressed is to try to identify those emission line sources that are not PNe, and to estimate what fraction of PNe we may have missed in the survey.

With only a single emission line detected by PN.S, any object that emits [O III] may form part of the data set (or, indeed, any object along the line of sight with a redshift that places an unrelated emission line at this wavelength). The dominant contaminating objects are likely to be H II regions, which emit strongly in [O III], and exist in large numbers in disk galaxies like M31. Most of these objects will already have been excluded, since their extended nature means that they will have been cut from the data set at the source-identification stage (even the largest PNe, with diameters of up to 3 pc, will be essentially unresolved in these data). However, H II regions have a broad size distribution, and the more compact ones will be barely resolved so will still be in the sample. Figure 16 shows the distribution of source sizes, normalised to the seeing, of the objects remaining in the survey; there clearly remains a tail of resolved objects, so we have flagged sources for which the FWHM normalised by seeing exceeds a value of 1.25 as probable H II regions in the final catalogue.

When examining the spatial distribution of the objects flagged by this process, it was found that they largely lie in a ring around M31's centre. A further clump of 35 objects was also found in a single field close to the centre of M31. This field was the only one close to the galaxy's centre that was observed under good seeing conditions ($\sim 0''.8$: see Figure 3). With the seeing this good, the

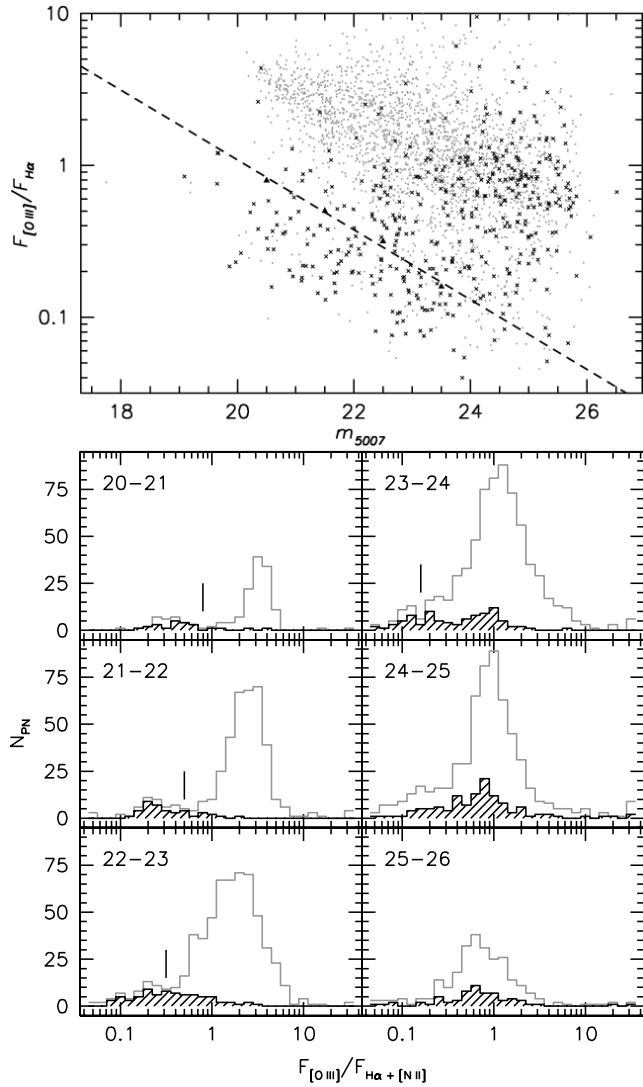


Figure 17. The flux ratio of [O III] to ($H\alpha + [N II]$) versus magnitude. The upper panel shows all the data, with extended objects shown as black crosses. The lower panel shows the same data as histograms in different magnitude bins, with the extended sources shaded. The vertical line in each histogram shows a suggested division between PNe and H II regions based on these distributions. These lines have been plotted as triangles in the upper panel, and the dashed line connects them.

variation in instrumental focus across the field and differences between the two PN.S images may become significant, so it is possible that these apparently extended objects are actually unresolved PNe. However, for consistency we also flag them as non-PNe; as discussed previously, we in any case do not expect the survey to be complete in these crowded high surface-brightness fields.

Presumably, this cut on angular size will still miss the most compact H II regions and in the central regions where the seeing was very poor objects with diameters of up to ~ 15 pc will be classified as compact by this cut. Fortunately, we do have some further information that we can use to try to identify these remaining contaminants. Specifically, we have measured fluxes from both the [O III] and ($H\alpha + [N II]$) lines from the M02 data, and the ratio of these fluxes, R , differs between PNe and H II regions (Ciardullo et al. 2004). In particular, since PNe give out most of their light in the [O III] line, we would expect R to be large for

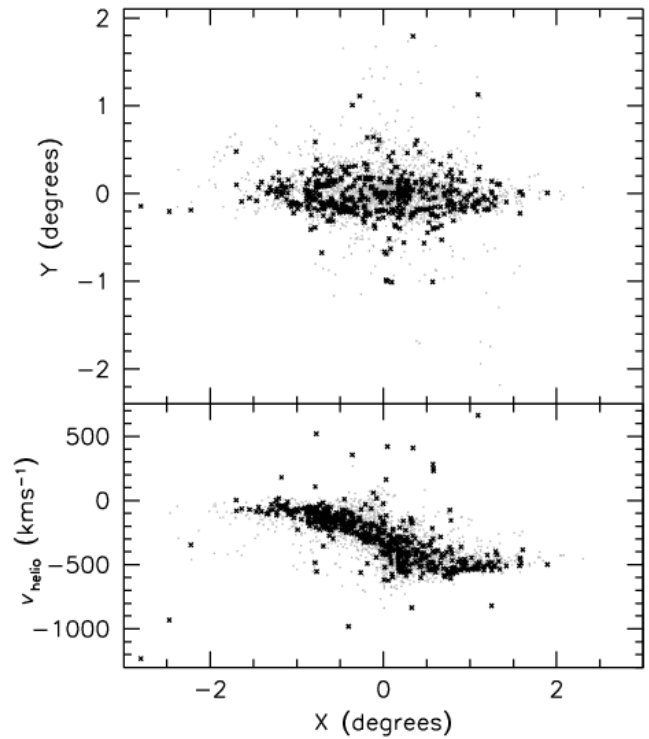


Figure 18. Locations in position and velocity of sources identified as probable H II regions. The whole sample is shown as small dots, with the probable H II regions as larger crosses.

these objects. Attempts have been made to quantify this criterion, leading to the suggestion that for bright PNe one should place a cut at $R \sim 1 - 2$ (Ciardullo et al. 2002, 2004; Magrini et al. 2000). However, it became clear when we started investigating this quantity for the data in the PN.S survey that the appropriate value for this cut varies significantly with magnitude. As Figure 17 illustrates, the optimum cut in R to exclude H II regions (as calibrated using the identified extended sources) decreases at fainter magnitudes. We have therefore applied the cut shown as a dashed line in Figure 17, with all sources below the line flagged as H II regions, regardless of their sizes. Although the distribution of extended sources on this plot would indicate that some fraction of the sources above this line are H II regions and this cut is lower than the ones made by Ciardullo et al. (2002, 2004) and Magrini et al. (2000), we have been chosen to be conservative by only selecting for exclusion the area of the plot that seems virtually devoid of PNe.

Figure 18 picks out the locations in the $\{X, Y\}$ and $\{X, v\}$ planes of the objects that these two criteria have identified as non-PNe. Although the criteria were designed to flag up probable H II regions, it is clear that they also exclude most of the objects with velocities that are inconsistent with membership of M31. Closer inspection shows that the majority of these sources have emission lines extended in the dispersion direction, indicative of Doppler broadening of the emission from massive background galaxies. We could, for example, be observing the redshifted $\lambda 3727 \text{ \AA}$ [O II] emission from star-forming galaxies at redshifts ~ 0.34 . Clearly, more extensive conventional spectroscopy would be required to confirm any such identifications. Figure 18 also shows the structure in the distribution of H II regions associated with spiral arms as well as the ring mentioned above. At a radius of 0.8° , the ring

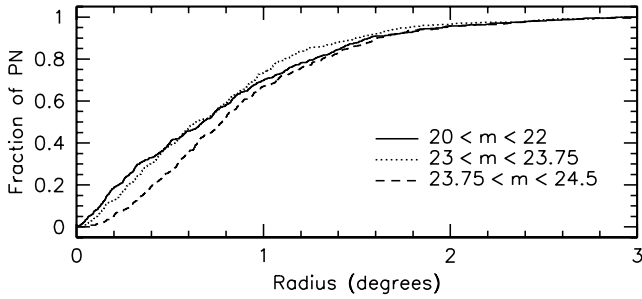


Figure 19. Cumulative distribution of radii in the disk plane for bright (solid line), intermediate-luminosity (dotted line) and faint (dashed line) PNe. A Kolmogorov-Smirnov test shows the distribution of bright and intermediate-luminosity PNe to be statistically indistinguishable at the 95% confidence level. There is a dearth of faint PNe near the centre of M31 resulting from poor seeing conditions and a high surface brightness.

coincides with the star-forming ring discussed by Devereux et al. (1994), where an excess of H II regions might be expected.

As a final check on our reliability in identifying contaminating sources, we have compared our identifications with the catalogue of 1312 emission-line objects that Meyssonier et al. (1993, hereafter MLA93) detected and classified in M31 using broader-band slitless spectroscopy. We find 856 of these objects to be within $4''$ of an object in our survey, the great majority of which are classified as PN by both MLA93 and ourselves. Only 94 of these objects are listed by MLA93 as non-PNe, and we have successfully flagged two-thirds of these as non-PNe as well. Of the remaining 31, MLA93 identify 25 as possible Wolf-Rayet stars. Since Wolf-Rayet stars are at a late stage in stellar evolution rather similar to PNe, and the two are sometimes even found together (Górny & Stasińska 1995), it is not clear that they should be considered as contaminants at all. One object classified as a possible QSO or Wolf-Rayet star is discussed further in Section 7. The last five objects are of uncertain classification in the MLA93 catalogue and will be left in this catalogue. The 456 objects that were not found presumably do not exhibit [O III] emission.

The other side to this coin is to ask how many PNe we might have missed. A simple test of completeness can be made by comparing the distribution of PNe with radius in different magnitude bins. As Figure 19 shows, bright and intermediate-luminosity PNe show spatial distributions that are statistically indistinguishable, but the faint PNe display a dearth of objects at small radii. As discussed above, such incompleteness is expected given a combination of the high surface brightness of the bulge region and the poor seeing conditions during observations of the central fields. Overall, we can tentatively conclude that the sample is complete to $m_{5007} = 23$ over the entire survey, to $m_{5007} = 23.75$ at projected disk radii larger than 0.2° , and to $m_{5007} \sim 25$ beyond 1° ; we will revisit this issue when we look at the PN luminosity function in Section 8. In terms of spatial coverage, as Figure 2 shows, M31 has been completely mapped out to a deprojected disk radius of 1.5° . Beyond that radius, the major and minor axes are somewhat unevenly sampled from one side to the other, but still with reasonable spatial coverage. Thus, although not spatially complete, useful kinematic information can be gleaned out to 2° (27.4 kpc).

6 THE CATALOGUE

Having calibrated the data spectroscopically, astrometrically and photometrically, both internally and against external results, we are now in a position to present the complete database from the survey. The full final version of the resulting data table of 3300 emission line objects including 2730 probable PNe is included in the electronic version of this paper, but Table 3 gives a small sample of the tabulated data listing coordinates, magnitudes, heliocentric velocities, whether the source is a probable PN, whether it lies in M31 (see Section 7), when the data were obtained, and cross-identifications with other catalogues.

7 SATELLITE GALAXIES AND OTHER OBJECTS IN THE PN.S SURVEY AREA

Within the area of this survey are a number of galaxies besides M31. Some of the objects in our catalogue which reside in these systems can be identified in the database because their velocities are far from that of M31. As we have seen above, most such sources have already been flagged as non-PNe because of their extended nature or low [O III]/H α ratio, and are probably in quite distant faint background systems. In some cases, such as the sources in the less-distant background galaxy Andromeda IV, there may be a few genuine PNe. Of more immediate interest are the satellite galaxies around M31. In these systems, we do detect quite a number of PNe, which means we can obtain some crude measure of the internal kinematics of these systems, but we must take some care in flagging these sources so that they do not compromise the use of this data set to model the dynamics of M31.

The locations of the known galaxies in the survey field are indicated in Figure 20, and we now consider them in turn, to try to identify the sources that lie within them, both on the basis of their positions and their velocities. Probable non-members of M31 identified in this way are annotated as such in the full database (see Section 6).

7.1 M32

M32 (NGC 221), is a compact dwarf elliptical galaxy (cE2) projected in line with the disk of M31. Its major and minor axes measure $\sim 8'.7$ and $6'.75$ in diameter respectively to a B-band magnitude level of 25.0 mag arcsec $^{-2}$ (de Vaucouleurs et al. 1991). It has a system velocity of -200 ± 6 km s $^{-1}$ (Huchra et al. 1999), and a velocity dispersion of 50 ± 10 km s $^{-1}$, rising to ~ 80 km s $^{-1}$ at its centre (Simien & Prugniel 2002).

We have considered all the emission-line objects in the PN.S survey within a $5'.7$ radius (1.5 times the mean 25.0 mag arcsec $^{-2}$ B-band radius) of the centre of M32 as candidate members of the satellite (see Figure 21). Using the PNe at somewhat larger distances from M32 to characterise the kinematics of M31's disk in this region, we find that a velocity cut at -350 km s $^{-1}$ (three times the measured dispersion from M32's systemic velocity) yields a reasonably clean division between the two systems. However, it is possible that a few of the PNe on the M31 side of the cut may be objects with the most extreme velocities in M32. To warn of this possibility, objects in the catalogue are flagged as "M32" if they meet the cut in velocity as well as position, and "M32?" if they are simply coincident with M32's location.

The sample of likely M32 PNe has only 46 members, so there

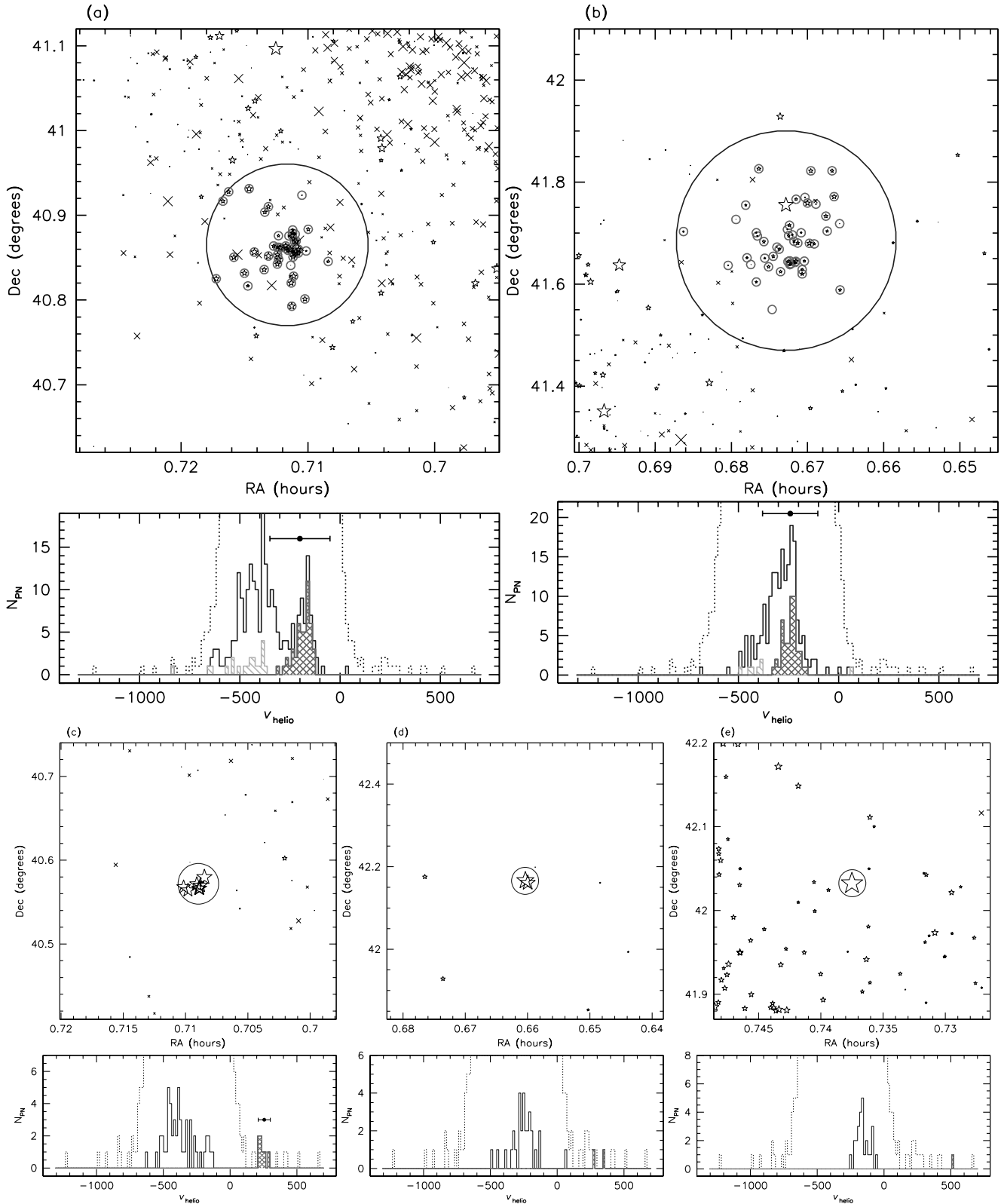


Figure 21. PN.S data in the vicinity of: (a) M32, (b) NGC 205, (c) And IV, (d) 2MASX J0039374+420956, (e) MLA93 0953. The area around each minor galaxy is shown in the upper panels. The sizes of each symbol indicate an emission-line object's velocity with respect to M31, with crosses showing negative values and stars showing positive values. The large circles indicate the approximate spatial extent of M32 and NGC 205 (1.5 times the mean 25.0 B-mag arcsec⁻² radius) and the location of the smaller galaxies. For M32 and NGC 205 PNe with circles around them have both position and velocity consistent with membership of that galaxy. The lower panels show velocity histograms, the dotted line being the whole PN.S sample, the solid line indicating an area including the minor galaxy but extending well beyond its optical extent, the hatched histograms showing the PNe within the area of galaxy, and the cross-hatching highlighting PNe that agree in velocity as well as position; the points indicate the smaller galaxy's systemic velocity (from the literature, if known), with $3\sigma_v$ errorbars.

Table 3. Emission line objects identified in the M31 survey. See electronic version for full table.

ID	RA J2000.0	Dec J2000.0	m_{5007}	v_{helio} km s^{-1}	Note a	Host b	Date	Field Number	H06 c	C89 c	HK04 c	MLA93 c
1	0:41:01.7	42:07:58.6	25.48	-283.3	-	-	2002.10.12	1	-	-	-	-
2	0:40:35.4	42:10:32.0	22.16	-133.9	-	-	2002.10.10	2	-	-	-	-
3	0:39:35.9	42:09:39.5	25.51	268.9	-	2MASXi	2002.10.10	3	-	-	-	-
4	0:39:37.3	42:09:59.6	23.52	354.5	E	2MASXi	2002.10.10	3	-	-	-	-
5	0:39:31.6	42:11:56.6	23.28	-343.3	-	-	2002.10.10	3	-	-	-	-
6	0:38:54.0	42:09:39.3	25.36	-266.7	E	-	2002.10.10	4	-	-	-	-
7	0:37:54.3	42:14:49.3	23.37	-328.1	-	-	2002.10.10	5	-	-	-	-
8	0:43:11.6	42:07:13.0	22.31	-194.0	-	-	2002.10.12	7	PN_10_3_1	-	-	-
9	0:43:10.5	42:11:33.3	23.58	-286.1	-	-	2002.10.12	7	PN_10_3_2	-	-	-
10	0:43:09.5	42:14:24.2	24.87	-314.2	-	-	2002.10.12	7	-	-	-	-
11	0:42:49.6	42:15:03.7	24.38	107.3	E	-	2002.10.12	7	-	-	-	-
12	0:44:08.6	42:06:00.0	25.62	-202.5	-	-	2002.10.13	8	-	-	-	-
13	0:44:09.8	42:06:40.2	22.99	-108.0	-	-	2002.10.13	8	PN_10_3_7	-	-	-
14	0:43:31.0	42:09:25.7	24.20	-136.6	-	-	2002.10.13	8	-	-	-	-
15	0:43:39.8	42:13:46.3	25.07	-210.8	-	-	2002.10.13	8	-	-	-	-
16	0:43:37.6	42:06:58.6	24.65	-554.4	E	Stream?	2002.10.13	8	-	-	-	-
17	0:44:59.8	42:07:44.8	21.76	-193.6	-	-	2002.10.12	9	PN_9_3_4	-	-	1091
18	0:45:00.9	42:08:44.8	23.53	-72.2	-	-	2002.10.12	9	-	-	-	-
19	0:44:30.5	42:08:55.2	22.36	-81.9	-	-	2002.10.12	9	PN_10_3_8	-	-	1005
20	0:44:51.4	42:09:34.2	23.81	-148.4	E,R	-	2002.10.12	9	-	-	-	-
⋮	⋮	⋮	⋮	⋮	⋮	⋮	⋮	⋮	⋮	⋮	⋮	⋮

^a Probable H II regions (or background galaxies): E – extended in the PN.S data, R – Flux ratio R below cutoff value (see Figure 17), other – excluded as a PN due to flux.

^b Sources of non-M31 objects: M32 / M32? – Objects associated with and in the vicinity of M32. NGC205 / NGC205? – Objects associated with and in the vicinity of NGC205. AndIV – Objects associated with the galaxy Andromeda IV. 2MASXi – Non-M31 source in the 2MASS catalogue. MLA93 – Non-M31 source listed in Meyssonier et al. (1993). NS – Objects in the region of the Northern Spur. Stream? – Objects referred to in Merrett et al. (2003) as being a possible extension of the Southern Stream.

^c cross-identifications from other catalogues: H06 – Halliday et al. (2006); C89 – Ciardullo et al. (1989); HK04 – Hurley-Keller et al. (2004) (format: table_ID); MLA93 – Meyssonier et al. (1993).

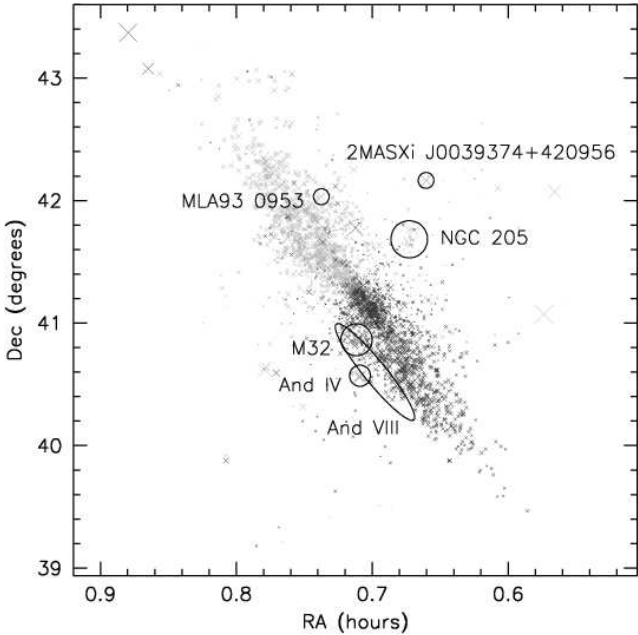


Figure 20. Positions of other galaxies and the detected emission line objects. An object's size and colour reflects its velocity with respect to M31's system velocity: grey objects are receding and black ones are approaching.

is not much that we can do in terms of detailed dynamical modelling. A simple Gaussian fit to the velocity distribution yields a mean velocity of $-174 \pm 6 \text{ km s}^{-1}$ and a velocity dispersion of $36 \pm 5 \text{ km s}^{-1}$. The mean velocity is not in particularly good agreement with the usually-adopted value; the difference seems to arise from the statistical coincidence that most of the PNe in M32 reside on one side of the galaxy's minor axis (see Figure 21), so the measured mean velocity contains an element of the system's rotation; the somewhat low value for the velocity dispersion is also consistent with this interpretation.

7.2 NGC 205

NGC 205 (M 110) is a dwarf elliptical galaxy (dE5) projected $\sim 35'$ from the centre of M31, close to its minor axis. Its major- and minor-axis diameters are $\sim 21'.9$ and $\sim 11'.0$ respectively at a position angle of 170° (de Vaucouleurs et al. 1991). It has a mean velocity of $v_{\text{NGC205}} = -241 \pm 3 \text{ km s}^{-1}$ (Bender et al. 1991), and a mean velocity dispersion of $\sigma_{\text{NGC205}} = 46 \pm 8 \text{ km s}^{-1}$ dipping to $\sim 20 \text{ km s}^{-1}$ at the very centre of the galaxy (Mateo 1998; Carter & Sadler 1990; Simien & Prugniel 2002).

To identify PNe in NGC 205, we have selected the objects within 12.3 of NGC 205's centre (1.5 times the mean $25.0 \text{ mag arcsec}^{-2}$ B-band radius), and applied velocity cuts at -375 km s^{-1} and -102 km s^{-1} to seek to isolate the galaxy's members. These velocity selections lie at approximately $v_{\text{NGC205}} \pm 3\sigma_{\text{NGC205}}$, although the lower bound is placed slightly high to avoid excluding

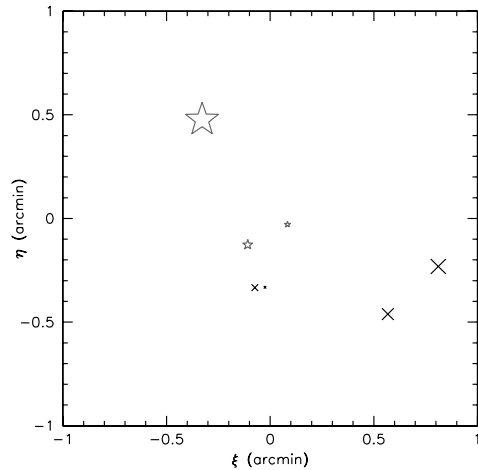


Figure 22. Kinematics of emission-line sources in Andromeda IV. The coordinates are defined relative to the centre of the satellite. Point sizes are proportional to velocity with respect to And IV, with grey stars and black crosses respectively representing positive and negative values respectively.

M31 PNe that are seen to have such velocities at slightly larger distances from NGC 205. As with M32, the possible overlap at these velocities means that there is unavoidably some ambiguity in the identification of satellite members, so Table 3 annotates those objects that meet the velocity constraints as “NGC205,” while those that are just spatially coincident are marked as “NGC205?” A Gaussian fit to the velocity distribution of likely members yields a mean velocity of $-235 \pm 6 \text{ km s}^{-1}$ and a velocity dispersion of $35 \pm 9 \text{ km s}^{-1}$, in agreement with the published values.

7.3 Andromeda IV

Andromeda IV is a background dwarf irregular galaxy lying a projected distance of $40'$ from the centre of M31. Ferguson et al. (2000) have previously identified a number of emission-line objects associated with this galaxy, and we list the cross-identifications in the current survey in Table 4. The only object that we fail to recover from the Ferguson et al. (2000) study is their “F1” source, which was originally detected in $H\alpha$, but has no [O III] counterpart in the magnitude range of our survey. The Ferguson et al. (2000) objects F7 and F8 are located a little away from the galaxy centre, and our measurements show that their velocities are consistent with the disk of M31, so they do not appear to be members of And IV, and they are excluded from the remaining analysis. Table 4 also adds two new emission-line sources to the list of objects with positions and velocities consistent with membership of And IV.

The resulting list of seven likely And IV members has a mean velocity of $241 \pm 10 \text{ km s}^{-1}$, in agreement with the published value of $256 \pm 9 \text{ km s}^{-1}$, as measured from spectra of only three sources (Ferguson et al. 2000). As Figure 22 illustrates, the velocities do not appear to be randomly distributed through the system, but indicate a line-of-sight component of rotation of $\sim 35 \text{ km s}^{-1}$ about a centre of $RA_0 \approx 0^{\text{h}}42^{\text{m}}32^{\text{s}}.3$, $Dec_0 \approx 40^{\circ}34'18''$.

7.4 2MASXi J0039374+420956

Two PN.S emission-line objects that exhibit velocities inconsistent with M31, one of which is extended, were found in the vicinity of this extended infrared 2MASS source (marked as 2MASXi in Table 3). The two objects lie at projected radii of $2''.8$ and $24''.2$ from

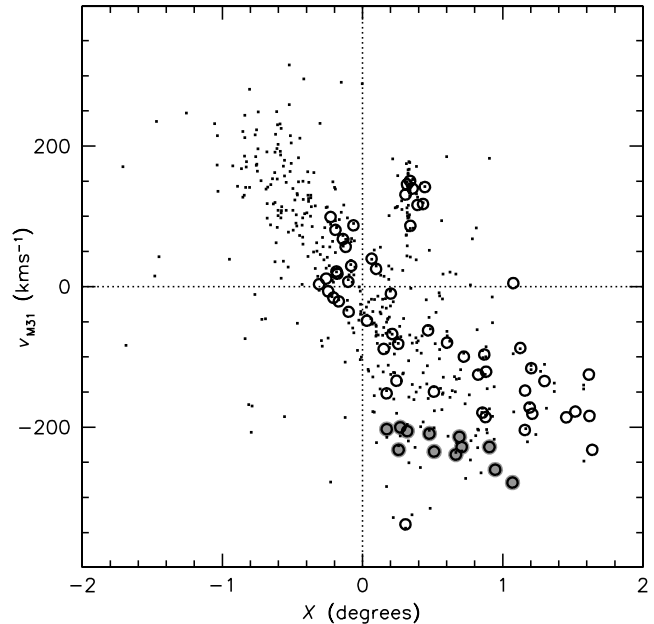


Figure 23. Plot of major-axis coordinate versus line-of-sight velocity, highlighting the postulated location of the And VIII satellite. The small dots show the PN.S survey data with Y coordinates between -0.175° and -0.450° , the region in which the known And VIII candidate PNe lie. The open circles are the Hurley-Keller et al. (2004) data set within the same slice in Y , with the highlighted points indicating the suggested members of And VIII.

the source centre. With only one emission line detected, we cannot unequivocally confirm its nature, but if we assume it originates from [O III], then this system would be placed at a heliocentric velocity of $\sim 300 \text{ km s}^{-1}$. As this velocity is similar to that derived for And IV, it is possible that both these galaxies belong to the same nearby background group. However, further observations would be required to confirm that this is the case.

7.5 MLA93 0953

One object with a velocity inconsistent with M31 was also listed in the Meyssonier et al. (1993) catalogue of M31 emission-line objects. They identified it as either a Wolf–Rayet star or a background QSO. Given our velocity measurement, it seems most likely that the object is a background QSO with an emission line that happens to lie within the [O III] bandpass.

7.6 Andromeda VIII

Morrison et al. (2003) pointed out a coincidence in position and velocity of a number of globular clusters and PNe from the Hurley-Keller et al. (2004) survey. These objects appeared to be quite well separated in velocity from both the modelled kinematics of M31’s thin disk in this region and the nearest other PNe, leading Morrison et al. (2003) to suggest that these sources might be providing the signature of a new tidally-distorted satellite galaxy in M31, Andromeda VIII.

However, as Figure 23 illustrates, with our larger sample of PNe this gap in velocities between the disk of M31 and And VIII is no longer devoid of PNe. The errors on the new velocities are somewhat larger than those previously published, but not sufficiently so to fill in the apparent $\sim 50 \text{ km s}^{-1}$ gap in the original smaller data

Table 4. Emission-line objects found in the vicinity of And IV, and comparison to the Ferguson et al. (2000) data set.

PN.S survey ^a						Ferguson et al. (2000) ^b		Notes
ID	RA	Dec	r	m_{5007}	v_{helio}	ID	v_{helio}	
2110	0:42:20.3	40:32:31.8	174	25.27	-386.7	F7		Below flux ratio cutoff, Belongs to M31
2111	0:42:35.3	40:33:51.0	44	24.14	219.2			Not found by Ferguson et al. (2000)
2112	0:42:21.2	40:33:50.0	130	21.74	-372.5	F8		Belongs to M31
2113	0:42:32.2	40:33:58.8	20	22.53	236.2	F3	244 ± 15	Extended
2114	0:42:36.6	40:34:04.8	51	23.47	213.3	F2		
2115	0:42:31.7	40:34:11.1	10	23.13	253.9	F4	250 ± 13	Extended
2117	0:42:32.7	40:34:17.0	5	25.20	248.8	F5		
2119	0:42:30.6	40:34:47.3	35	24.43	285.7	F6	273 ± 19	Extended
2128	0:42:31.9	40:33:58.7	20	24.79	228.5			Not found by Ferguson et al. (2000)
	0:42:37.6	40:38:12	241			F1		Not found in PN.S survey

^a ID, RA, Dec, m_{5007} and v_{helio} from Table 3 except object F1, which was not detected. r is the objects radial distance from And IV measured in arcseconds.

^b ID and velocity from Ferguson et al. (2000) Tables 1 and 2.

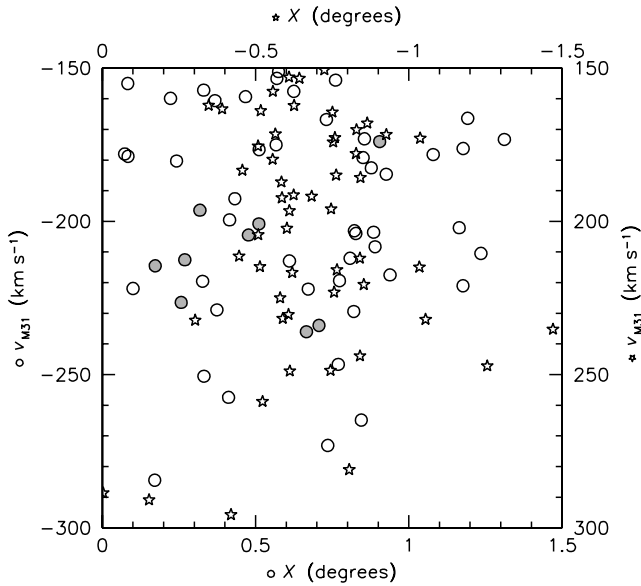


Figure 24. Overlay of the major-axis coordinate versus line-of-sight velocity for the PN.S data in the location of And VIII (circles) and the equivalent phase-space location on the opposite side of M31 (stars). The PNe previously identified as possible And VIII members are highlighted in grey.

set. Perhaps more tellingly, Figure 24 shows that the equivalent region on the opposite side of M31 contains a very similar distribution of PNe. In fact the equivalent regions in all four quadrants of M31 are similarly populated by PNe. We therefore conclude that while these PNe may not be members of M31's thin disk, they do probably constitute a normal component of the system's PN distribution, and it is not necessary to invoke the external explanation of a tidally-distorted dwarf companion.

7.7 Other objects flagged in the PN.S catalogue

On the basis of the analysis in this section, all objects whose kinematics are inconsistent with M31 have either been identified with known satellites, or they have been previously flagged as non-PNe on the basis of their extended nature or line ratios (see Section 5). The only other source that we flag as likely not an M31 PN is object 2654. Although this source's kinematics and position are consis-

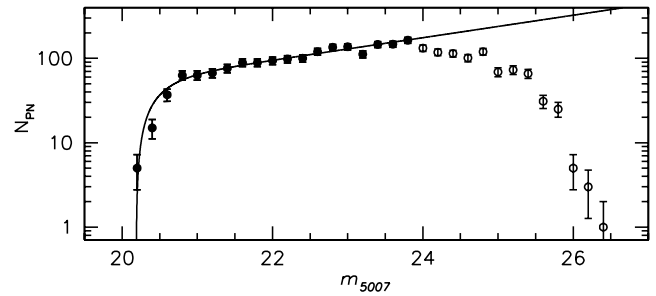


Figure 25. The planetary nebula luminosity function of M31 as derived from the current survey. Filled circles are plotted up to the magnitude completeness limit; open circles are shown beyond this point.

tent with membership of M31, it is nearly 0.4 magnitudes brighter than any other PN in M31. Unfortunately, it lies outside the region mapped by Massey et al. (2002)'s imaging, so we do not have the line ratio diagnostic as a further discriminant. However, given the very sharp cut-off in the PN luminosity function (see Section 8), it is most unlikely that this object is a PN, so we flag it in the catalogue and exclude it from the following analysis.

8 THE PLANETARY NEBULA LUMINOSITY FUNCTION

Planetary nebulae are observed to follow a well-defined luminosity function of the form

$$N(M_{5007}) \propto e^{0.307M_{5007}} \left(1 - e^{3(M_{5007}^* - M_{5007})} \right) \quad (9)$$

(Ciardullo et al. 1989), with an equivalent formula for apparent magnitudes for any individual system. The absolute magnitude of the bright-end cutoff, M_{5007}^* , has a surprisingly universal value of -4.5 , varying only weakly with the host galaxy metallicity (Ciardullo et al. 2002). Figure 25 shows the PNe from this survey, with non-members of M31 removed, fitted by this function. As the figure shows, this functional form fits very well all the way to our completeness limit of $m_{5007} = 23.75$. The apparent magnitude of the bright end cutoff, for the sample is $m_{5007}^* = 20.2 \pm 0.1$. This result is in excellent agreement with the value published by Ciardullo et al. (1989) of 20.17.

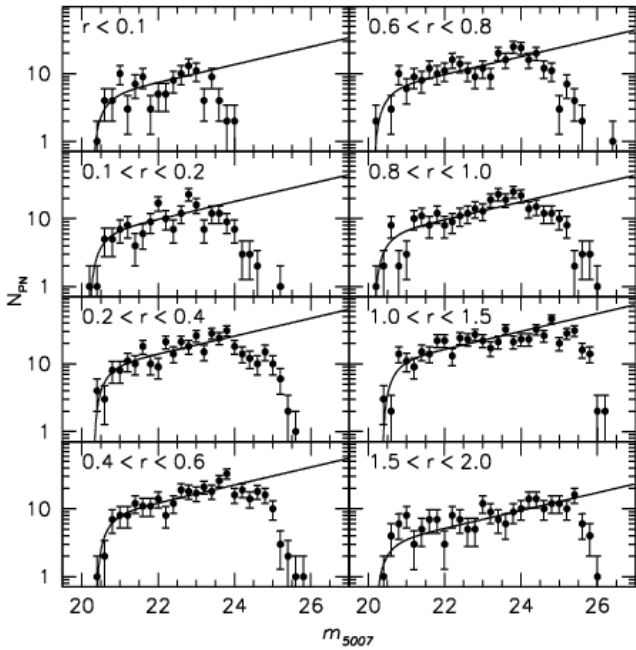


Figure 26. The planetary nebula luminosity function at different deprojected disk radii in M31.

The large number of PNe in our survey means we can divide up the planetary nebula luminosity function (PNLF) and examine it at different points within the galaxy to test the universality of its form. PNLFs for sections at different deprojected disk radii are shown in Figure 26. The positional variation in the completeness of the survey is clearly shown in this figure: as discussed above, the high surface brightness and poor seeing of the central fields mean that these data are only complete to $m_{5007} \sim 23$. For radii between 0.2° and 1.0° , incompleteness becomes apparent at $m_{5007} \sim 24$, while at the largest radii, for which we used the best seeing conditions (see Figure 3), we are close to complete at $m_{5007} \sim 25$.

Recent observations of PNe in the SMC (Jacoby & De Marco 2002) and M33 (Ciardullo et al. 2004) have detected deviations from the simple monotonic function of equation (9). In these objects, dips have been observed in the PNLF, whose origins have been proposed as resulting from a recent star formation episode. The only indication of a dip in the PN.S data set is the point at 23.2 mag in Figure 25 which lies $\sim 2.5\sigma$ from the model value. It is interesting to note from Figure 26 that most of the signal responsible for this dip comes from the radial range $0.6^\circ < r < 0.8^\circ$ where the data dips $\sim 2\sigma$ below the model value at 23.2 mag. This is coincident with the star formation ring where the majority of H II regions are located discussed in Section 5, suggesting that star formation may be responsible for this marginally-detected feature as well.

More radically, Marigo et al. (2004) have suggested that the brightest PNe all originate from intermediate-mass stars, so that the bright end of the PNLF should vary dramatically between spheroidal and disk populations. The absence of any significant variation in M31's PNLF with radius, as one goes from the bulge-dominated to the disk-dominated parts of the galaxy, implies that no such effect is seen in this system.

As a further test of the universality of the PNLF, and to search for the effects of obscuration, we have also divided the data according to whether it comes from the near side (positive Y) or far side

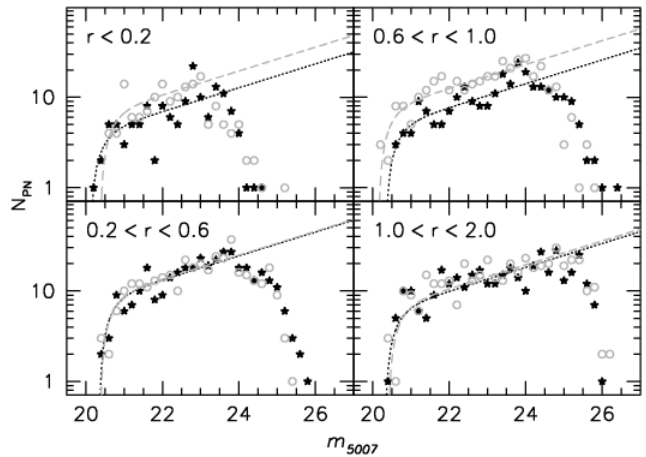


Figure 27. The planetary nebula luminosity function on the near and far side of M31 over different radial ranges. Black stars and the dotted line represent the data and fit to the near side of M31 (to the north-west), while grey circles and the dashed line show the corresponding information for the far side (to the south-east).

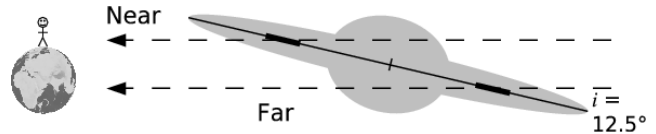


Figure 28. An illustration of the location of an Earth based observer with respect to the disk of M31. The dust lane is shown as the thick lines in the disk plane. On the near side of the disk the majority of light comes from behind the dust lane while opposite is true for the far side. Not to scale.

(negative Y) of the disk. As Figure 27 illustrates, at most radii the PNLFs are statistically indistinguishable. However, once again in the region of the ring at $0.6^\circ < r < 1.0^\circ$, we do see a small but significant difference, with the PNLF from the near side systematically fainter than that from the far side: values of the best fit for m_{5007}^* on the near and far side are 20.34 and 20.15 respectively. This rather counter-intuitive difference can be qualitatively explained if the ring of star formation also contains a modest amount of dust obscuration (Walterbos & Kennicutt 1988; de Jong et al. 2005). As Figure 28 shows, on the far side of the disk, the line of sight of an observer through a highly inclined system like M31 passes through more of the galaxy in front of the dust layer than behind, while the opposite is true on the near side. Hence on the near side of the disk most of the PNe observed are located behind the dust layer, dimming the PNLF relative to that seen on the far side. The lack of similar differences between other parts of M31 suggests that obscuration is not a major issue across most of the galaxy.

9 SPATIAL DISTRIBUTION OF PLANETARY NEBULAE

In order to interpret the kinematics of the PNe in this survey, we need to know what stellar population or populations these objects are tracing. It is generally assumed that PNe all originate from low-to-intermediate mass stars, so they should mainly trace the old stellar population, but, as we have discussed in Section 8, it has been suggested that some fraction of PNe originate from more massive stars. As a further test of this possibility, we can compare the distribution of PNe with that of the red light from the galaxy, which

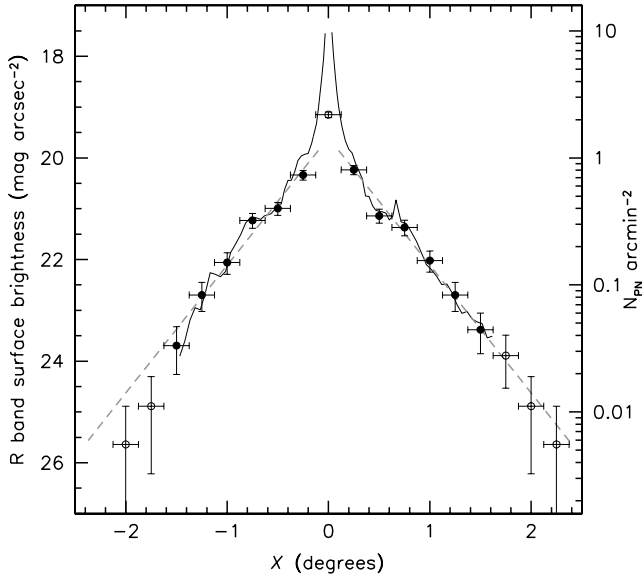


Figure 29. Surface brightness profile and PN number counts along the major axis of M31. The solid line shows the R-band surface brightness profile of Walterbos & Kennicutt (1987), and the dashed line is an exponential profile with a scale length of $0^{\circ}.43$ (Walterbos & Kennicutt 1988). The number density of PNe with $m_{5007} < 24$ is indicated by closed circles where the survey is complete both spatially and to $m_{5007} = 24$; open circles are used elsewhere.

we would expect to be dominated by relatively low-mass red giants, and hence would only be expected to follow the distribution of PNe if they originate from similar low-mass systems. To this end, we have obtained the radial distribution of the PNe with $m_{5007} < 24$ (the completeness limit of most of the survey) along the major and minor axes of M31.

Along the major axis, Figure 29 shows excellent agreement between the number counts of PNe and the R-band photometry of Walterbos & Kennicutt (1987). Fitting an exponential function to the distribution of PNe beyond the bulge and out to 1.6° yields a scale-length of $R_d = 0.43 \pm 0.02^{\circ}$ (5.9 ± 0.4 kpc), also in excellent agreement with the R-band value of $0.43 \pm 0.02^{\circ}$ (Walterbos & Kennicutt 1988). There are no indications of any cut-off in the exponential disk out to the limit of the survey at $\sim 5R_d$.

Figure 30 shows a similar plot for the minor axis. Once again, there is a good match to the published R-band photometry outside the central region, including reproducing the bump at $Y \sim 0.6^{\circ}$ due to NGC 205. The PNe also follow the published $R^{1/4}$ profile fit to the photometry with a bulge effective radius of $R_{\text{eff}} = 0^{\circ}.10$ (1.4 kpc) (Irwin et al. 2005). Even at $\sim 10R_{\text{eff}}$, there are no signs of an excess over this fit, and hence no evidence for a separate halo population even at these very faint surface brightness levels (equivalent to ~ 26 mag in the R band).

It thus appears that the PNe trace the same stellar population as the old stars seen in the galaxy's red light. They also seem to broadly fit a simple two-component model comprising an $R^{1/4}$ central bulge and an exponential disk out to the very faint surface brightness levels accessible using such discrete dynamically-selected tracers.

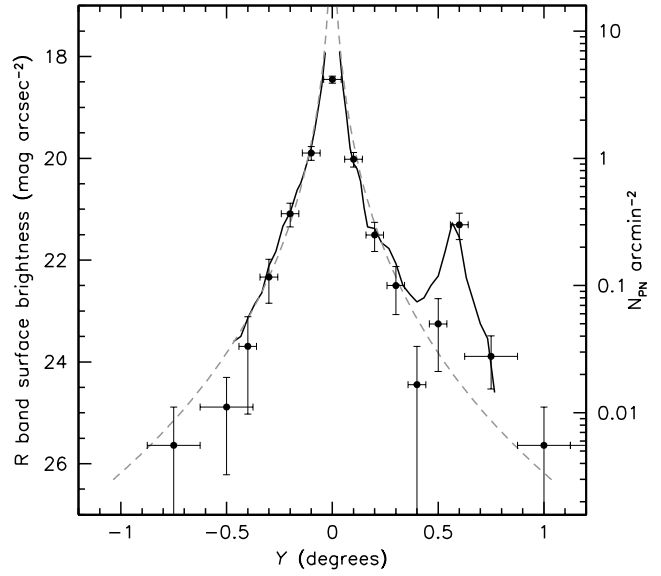


Figure 30. Surface brightness profile and PN number counts along the minor axis of M31. The solid line is the R-band surface brightness profiles of Walterbos & Kennicutt (1987), and the dashed lines is the $R^{1/4}$ profile fit to the photometry by Irwin et al. (2005). The number density of PNe with $m_{5007} < 24$ is indicated by the filled circles.

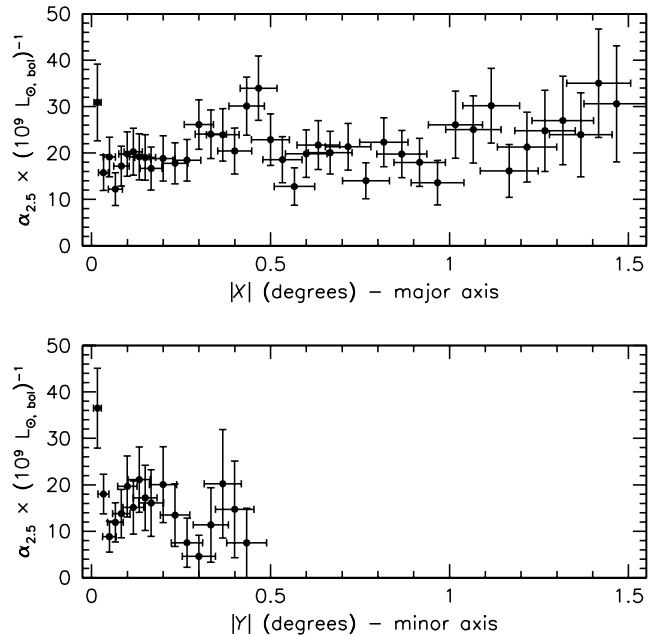


Figure 31. Variation of $\alpha_{2.5}$ with distance along the major and minor axes. $\alpha_{2.5}$ is estimated at positions along the two axes where Walterbos & Kennicutt (1987) list a value for the surface brightness, the number density of PNe at each location is estimated from the number of PNe in a box whose dimensions are equal to the horizontal error bar.

10 THE LUMINOSITY-SPECIFIC PN DENSITY

Having established the proportionality between the stellar continuum emission and the distribution of PNe, we now turn to the constant of proportionality. This quantity, the luminosity-specific PN number density, is usually parametrised by the number of

PNe in the top 2.5 magnitudes of the PN luminosity function per unit bolometric solar luminosity, and is given the symbol $\alpha_{2.5}$

The bolometric luminosity of any part of M31 can be calculated via the standard relations

$$M_{bol} = M_V + BC_V \quad (10)$$

and

$$\frac{L_{M31,bol}}{L_{\odot,bol}} = 10^{-0.4(M_{M31,bol} - M_{\odot,bol})}, \quad (11)$$

where BC_V is the V-band bolometric correction which has a value of -0.80 mag for M31 (Ciardullo et al. 1989). The solar absolute bolometric magnitude, $M_{\odot,bol}$, is taken to be $+4.74$ mag (Cox 2000).

The number density of PNe along the major axis and the V-band photometry of Walterbos & Kennicutt (1987) [correcting to absolute magnitudes using $A_V = 0.206$ (Schlegel et al. 1998) and a distance modulus of 24.47] give an average value of $\alpha_{2.5} = (21 \pm 1) \times (10^9 L_{\odot,bol})^{-1}$. As Figure 31 shows, outside the very uncertain central bin there is no strong evidence for any gradient in the value of $\alpha_{2.5}$ with position, as we would expect on the basis of the close proportionality determined in the previous section. The same calculation on the minor axis, where the light profile is dominated by the bulge, gives $\alpha_{2.5} = (15 \pm 2) \times (10^9 L_{\odot,bol})^{-1}$, once again with no evidence for a gradient (see Figure 31). This value agrees very well with the calculation by Ciardullo et al. (1989) for the PNe in M31's bulge, from which they derived a value of $\alpha_{2.5} = 16.3 \times (10^9 L_{\odot,bol})^{-1}$.

The modest difference between the mean values for the minor and major axes is consistent with the existing evidence that $\alpha_{2.5}$ is correlated with galaxy colour, with red ellipticals being poorer in PNe per unit luminosity than blue spiral galaxies (Peimbert 1990; Hui et al. 1993); here for the first time we are seeing evidence for such a difference between spheroidal and disk components within a single galaxy. Fortunately, such a mild deficit in the number of PNe from the bulge component relative to those from the disk will have little impact on the dynamical modelling of these data, since it merely changes the effective normalisation of the number density of tracers in these two discrete components. We can therefore proceed to make a preliminary study of the PN kinematics in M31.

11 PLANETARY NEBULA KINEMATICS

In Figure 32, we show a plot of PN velocity against major axis position. A number of fairly subtle dynamical features are apparent in this plot. For example, many of the satellite galaxies identified in Section 7 (shown here as circles) stand out quite clearly. Similarly, the PNe identified by Merrett et al. (2003) as a possible continuation of the merging Southern Stream of stars (Ibata et al. 2001, 2004; McConnachie et al. 2003), shown as triangles, are apparent. Interestingly, the other strong photometric structure, the Northern Spur (Ferguson et al. 2002), does not stand out in the plot. The kinematics of PNe in this region (shown as squares in Figure 32) are indistinguishable from those of the disk, despite the Northern Spur's location some distance from the plane. It would thus appear that this feature is related to the disk, perhaps indicative of a warp. After these minor features have been excluded, Figure 32 shows that the kinematics are dominated by rotation at large radii, but that at small radii there is a larger random component, attributable to a bulge population. This result indicates that the majority of the PNe form a relatively simple system of rotationally-supported disk and

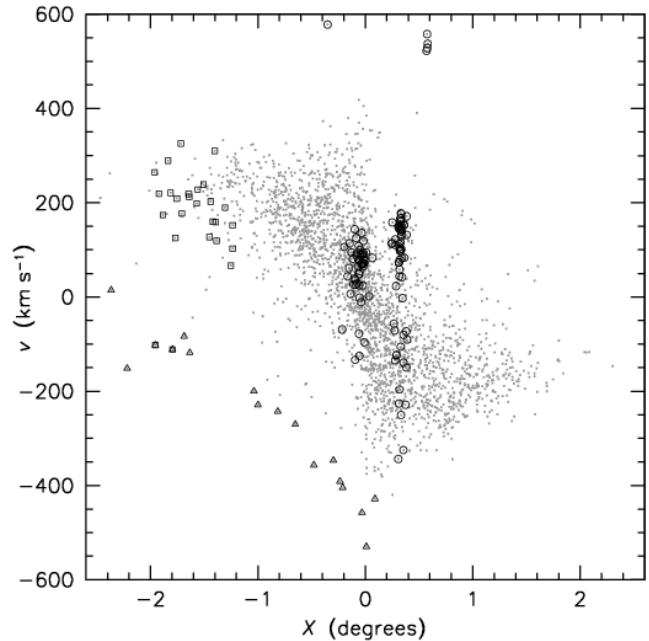


Figure 32. Scatter diagram of position along the major axis of M31 versus velocity for all the survey PNe. The highlighted objects are those in the region of satellite galaxies (circles; see Section 7); those in the region of the Northern Spur (squares); and those identified as forming a continuation of the Southern Stream (triangles).

randomly-supported bulge, in agreement with the conclusion based on photometry in Section 9.

A full dynamical model fit to the entire dataset is beyond the scope of this paper, but we can obtain some interesting insights by considering the PNe that lie close to M31's major axis. For a highly-inclined galaxy like M31, the observable kinematics in this region are dominated by the rotational motion, so we can essentially isolate this component of velocity. Accordingly, we have selected a sample of 690 PNe with $|Y| < 0^{\circ}.04$, close to the major axis. Figure 33 shows a plot of this subsample's line-of-sight velocities versus major axis position, together with the mean velocities derived by radially binning these PNe into groups of 50 objects. A system velocity of -309 km s^{-1} has been adopted as discussed previously.

The distribution of PN velocities in Figure 33 has an upper envelope that matches the rotation curves derived from various tracers (also shown in this figure) reasonably closely at large radii. At small radii, the PNe show a wide spread in velocities, indicative of a contribution from the bulge. It is also interesting to note the dip in the mean rotation speed of PNe at $\sim 0^{\circ}.3$. This feature, which shows up even more clearly in the CO rotation curve, has been attributed by Loinard et al. (1995) to non-circular motions associated with a barred bulge. Its appearance in the PNe kinematics confirms that they are dominated by disk objects even at this fairly small radius, but also serves as a warning that large non-circular motions may complicate the observed dynamics at these radii. At larger radii, the mean velocities of the PNe trace the rotation curve relatively well, except that the mean velocity lies systematically below the circular speed. We will return to the origins of this asymmetric drift in the mean velocities of PNe in Section 11.2, but first we look in more detail at their random motions.

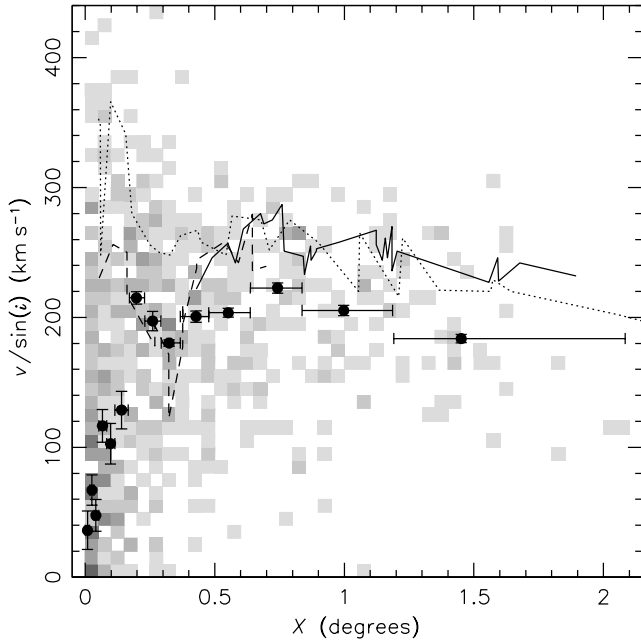


Figure 33. Plot of position versus velocity for PNe close to the major axis of M31 ($|Y| < 0^\circ 04$). The data from both sides of the galaxy have been combined, and the velocities have been corrected for the galaxy’s inclination. The grey-scale shows the density of PNe in this phase-space projection. The circles show the mean velocities of these data in a number of bins – the horizontal error bars show the extent of each bin, and the vertical bars the uncertainty in mean velocity. The dotted line shows M31’s H I rotation curve (Braun 1991); the dashed line shows the rotation curve derived from CO measurements (Loinard et al. 1995); and the solid line shows a rotation curve derived from H II region velocities (Kent 1989).

11.1 Velocity dispersion

Figure 34 shows the observed velocity dispersion as a function of position along the major axis obtained from the PNe in Figure 33, binned radially into groups of 50 objects. Near the centre, the calculated PN velocity dispersions agree well with the declining profile derived by McElroy (1983) from stellar absorption lines (also shown in the figure), providing further confidence in the PN results. However, the stellar absorption-line data only reach to $\sim 0.2^\circ$, while the PN profile goes out to $\sim 2^\circ$ (27.4 kpc). It is in these previously-unexplored outer regions that the velocity dispersion starts to behave a little strangely. First, there is a dip in the observed dispersions at $\sim 0.3^\circ$, suggesting that the bar’s influence shows up in the dispersion profile as well as the mean rotational velocity. Second, the dispersion profile seems to flatten out at larger radii to a constant value of $\sim 55 \text{ km s}^{-1}$. Ignoring the bar-related dip, a simple empirical fit to the large-scale profile, plotted as a grey dot–dash line in Figure 34, is given by

$$\sigma_\phi = \sigma_A + \sigma_B \exp\left(-\frac{R}{R_d}\right). \quad (12)$$

with $\sigma_A = 47 \text{ km s}^{-1}$, $\sigma_B = 84 \text{ km s}^{-1}$ and $R_d = 0^\circ 43$. Other recent stellar kinematic data from large radii also reveal significant dispersions: Ibata et al. (2005) find velocity dispersions of RGB stars of $\sim 30 \text{ km s}^{-1}$ from small fields at even larger distances along the major axis.

These results are not consistent with the expectations of the simplest disk models. By applying the tensor virial theorem to a one-dimensional sheet approximation to the vertical distribution of

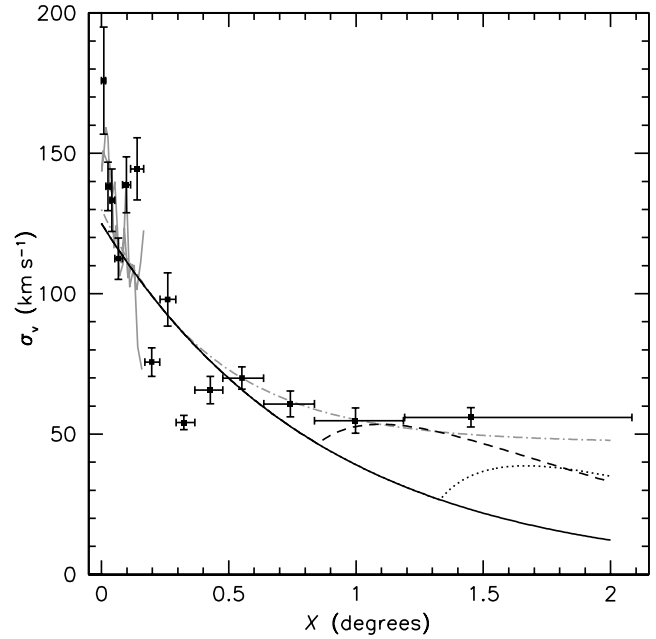


Figure 34. Velocity dispersion profile for the major-axis PN sample shown in Figure 33. Points with error bars show the binned PN dispersion profile, corrected in quadrature for the uncertainty in the PNe velocities. The solid grey line is the inner stellar velocity dispersion profile of McElroy (1983). The curves are for a number of models fit to the PN data with a χ^2 minimisation: the grey dot–dash line shows the empirical fit of equation (12); the solid black line shows a simple exponential decrease; the dotted black line is for a flaring disk model with parameters from Brinks & Burton (1984); and the dashed black line shows a flaring disk model with parameters matched to the PN velocity dispersion profile.

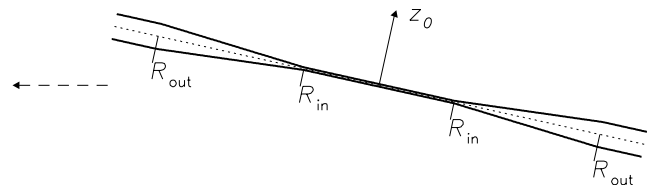


Figure 35. Schematic diagram of the flaring disk of M31. The disk scale height is constant out to a radius R_{in} it then increases linearly with radius to R_{out} , at which point it becomes constant again.

stars in a disk, one can show that the vertical velocity dispersion, σ_z , should be given by an equation of the form

$$\sigma_z^2 = 2\pi G \Sigma z_0 \quad (13)$$

where z_0 is the scale height and Σ the surface density of the disk (Binney & Merrifield 1998, p.727). If the surface density of stars drops off exponentially with radius with a scale-length R_d , and the scale-height stays constant with radius, then σ_z should drop exponentially to zero with a scale-length of $2R_d$. If the velocity ellipsoid remains roughly constant in shape, then the other components, including the observed ϕ component, should decrease in the same way. As the solid line in Figure 34 shows, this is not what we find in M31.

So, where have we gone wrong? Well, it is known that the outer parts of M31’s disk are not a simple constant-thickness flat sheet. The outer H I disk is significantly warped (Brinks & Shane 1984), and Brinks & Burton (1984) have suggested that the thickness of the H I layer also flares to greater scale-heights at large radii.

Their model for the flaring, shown schematically in Figure 35, assumes that the H I scale-height is constant at $z_{\text{in}} = 0^{\circ}01$ (136 pc) out to $1^{\circ}33$ (18 kpc), then increases linearly out to $R_{\text{out}} = 2^{\circ}54$ (34.5 kpc) where $z_{\text{out}} = 0^{\circ}14$ (1.9 kpc). Beyond this radius the H I becomes undetectable, but Ibata et al. (2005) have assumed the disk scale height becomes constant from this point onwards to account for their stellar observations.

If the scale-height increases in this way, then equation (13) implies that, for a given mass density, the vertical velocity dispersion also increases. If we insert the above prescription for the scale-height into this equation, but continue to assume that the disk density drops exponentially with radius, then we find the velocity dispersion profile shown as a dotted line in Figure 34. Although a step in the right direction, the fit to the observed profile is still not very good. Of course, there is no reason why the stellar disk, having been built up over an extended period and undergone secular heating since it formed, should flare in the same way as the H I distribution. Indeed, it is often assumed that the stellar scale-heights of disk galaxies remain constant with radius. However, recent analysis has shown that existing photometric data do not rule out significant variation in scale-height with radius (Narayan & Jog 2002). Further, if a disk comprises two components of different constant scale-heights, with the “thick disk” having a longer scale-length than the “thin disk,” then one would expect a variation with radius in their combined effective scale-height similar to this simple flaring model. Whether such components should be combined or should be considered as discrete entities is largely a matter of semantics unless one can establish some other feature that distinguishes their constituent stars. If we use this toy varying-scale-height model, but move the point at which the flaring starts to $R_{\text{in}} = 0^{\circ}85$ (11.6 kpc) while leaving all the other parameters unaltered, we obtain the dashed line in Figure 34, in respectable agreement with the data. Clearly, by altering the way in which the layer flares, or by varying the mass-to-light ratio of the disk with radius, we could improve the fit still further, but such detailed modelling goes beyond what is justified by the simplifying approximations of a one-dimensional sheet of stars in hydrostatic equilibrium.

11.1.1 Variation with magnitude

This analysis of the velocity dispersion allows us to make a further search for any systematic variation in the properties of PNe with luminosity. Such a test is motivated by knowledge of the Solar neighbourhood of the Milky Way, where we know that the tangential components of the velocity dispersions of different types of star vary by more than a factor of two, with the youngest, most massive stars having the lowest dispersions (Binney & Merrifield 1998). If the PNe in M31 that populate different parts of the PNLF had progenitor stars with very different masses, then we might expect similar variations in their velocity dispersions. Not only would such a variation fit with the suggestion of Marigo et al. (2004) that the bright end of the PNLF is populated by more massive stars, but it would also resonate with the recent claim by Sambhus et al. (2006) that the PNe in NGC 4697 can be divided on the basis of their luminosities into two discrete populations with distinct kinematics.

To test for such an effect, we have extracted from the major-axis subsample those objects for which $X > 0.3^{\circ}$: since the global velocity dispersion is approximately constant at these radii (see Figure 34), we can combine data across this range to form a meaningful average. Figure 36 shows the velocity dispersions determined from these data combined into half-magnitude bins. Clearly, there is no evidence for an decrease in dispersion for brightest ob-

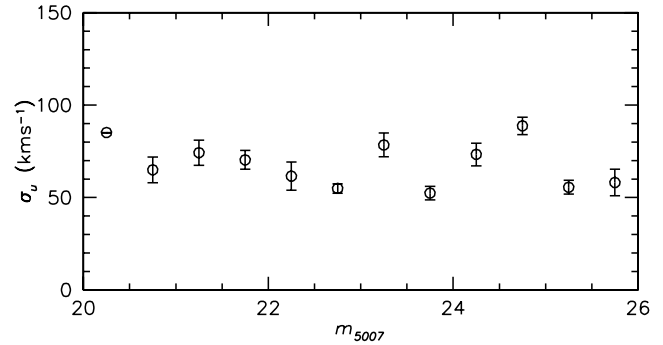


Figure 36. Variation in velocity dispersion with apparent magnitude for the major-axis data from the disk region at $X > 0.3^{\circ}$.

jects, adding further weight to the conclusion that PNe of all magnitudes form a relatively homogeneous population of old stars.

11.2 Asymmetric drift

The presence of significant random velocities at all radii means that the support against gravitational collapse does not come entirely from circular motions even at large distances from the centre of M31. We would therefore expect the observed mean rotational streaming of the stars, \bar{v}_ϕ , to lag behind the circular speed, v_c . As noted above, such an asymmetric drift is seen, but having measured the velocity dispersion profile we can now quantify whether the predicted velocity difference is dynamically consistent with the observations.

The relationship between \bar{v}_ϕ and v_c at any radius R is given by the appropriate axisymmetric Jeans equation (Binney & Tremaine 1987, equation 4-33), which we can rewrite as

$$\bar{v}_\phi = \sqrt{v_c^2 - \sigma_\phi^2 + v_R^2 + \frac{R}{\nu} \frac{\partial(\nu v_R^2)}{\partial R} + R \frac{\partial(\bar{v}_R v_z)}{\partial z}}, \quad (14)$$

where we have adopted a cylindrical coordinate system, $\{R, \phi, z\}$, and measure stellar velocities $\{v_R, v_\phi, v_z\}$ and number density $\nu(R, z)$ in this reference frame. To solve this equation, we have to make some further assumptions. First, the final term, which arises from any tilt in the velocity ellipsoid, is unobservable. However, for all plausible dynamical models it remains small and has little impact on an analysis of this kind (Gerssen et al. 1997), so we can safely neglect it. Second, we must assume something about the shape of the velocity ellipsoid of random motions. The simplest assumption is that it remains constant with position, so that we can write

$$\frac{\bar{v}_R^2}{v_R^2} = \alpha \sigma_\phi^2, \quad (15)$$

where α is a constant. In the solar neighbourhood of the Milky Way, α is found to be ~ 2 (Binney & Merrifield 1998), and in the absence of any other constraint we set it to this value at all radii in M31 (varying α by ± 0.5 makes little difference to the final result). If we make this approximation, use the H I data to obtain a simple linear approximation to the rotation curve $v_c(R)$, take the number counts of PNe in Section 9 to give the exponential disk distribution for $\nu(R)$, and use the smooth approximation to $\sigma_\phi(R)$ of equation (12), then we can substitute these quantities into equation (14) to predict the value of \bar{v}_ϕ .

To compare this value to the observed mean streaming of stars, we must make a couple of corrections to the model. The first is due to the inclination of the galaxy, but M31 is sufficiently close

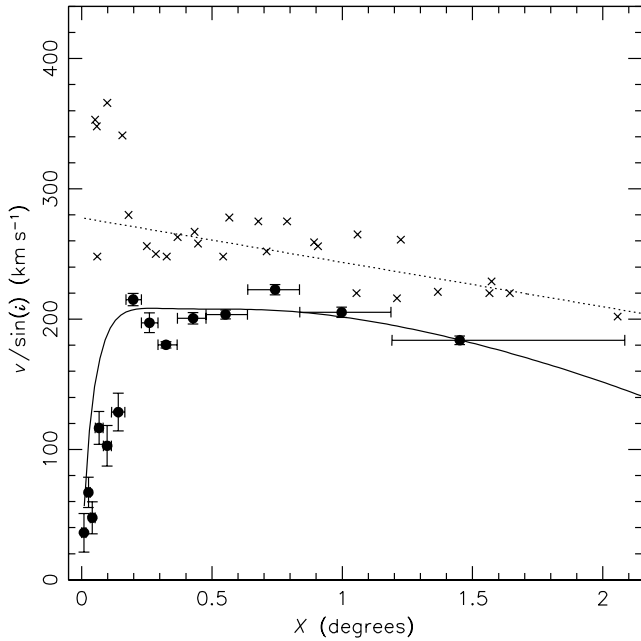


Figure 37. Predicted and observed rotational motions of PNe in M31. The filled circles show the observed streaming of stars, as in Figure 33. The crosses give M31’s H I rotation curve as derived by Braun (1991), with the straight line fit to the data used in this analysis shown by the dotted line. The solid line shows the predicted rotational velocity obtained by solving equation (14).

to edge-on that this effect is relatively minor and has already been accounted for in the data of Figure 33. The second effect is more significant: although we have selected a sample of PNe whose positions lie close to the major axis of M31, the cut at $|Y| < 0^{\circ}04$ does sample a range of azimuths, particularly at small radii. We have allowed for this effect by averaging the line-of-sight component of \bar{v}_{ϕ} in the model over the range of azimuths admitted at each position X along the major axis.

The net result of this calculation is shown in Figure 37. At small radii, the detailed match between model and observation is not perfect, but discrepancies here are not surprising since many of the PNe in this region will belong to the bulge rather than the disk as modelled here; even PNe from the disk will have their kinematics affected by the bar, which also has not been accounted for in this simple axisymmetric picture. At larger radii, however, the agreement is remarkably good. It should be stressed that this model has not been fitted to the data: the amplitude of the asymmetric drift between \bar{v}_{ϕ} and v_c is entirely fixed by the Jeans equation once we have determined the other quantities in this equation as described. Note also that although we have constructed this dynamical model by assuming the scale-height of M31’s disk population increases with radius, the absence of σ_z in equation (14) means that the agreement is not dependent on this specific model. All that is required is that the radial and tangential kinematics are coupled via equation (15); if σ_z is not coupled to these motions, then any scale-height can be accommodated. The generic agreement between model and data therefore provides a healthy consistency check on this analysis, and leaves us with a relatively simple self-consistent picture of the dynamics of M31’s surprisingly warm disk.

12 CONCLUSIONS

Using the Planetary Nebula Spectrograph, we have surveyed a wide area over the Andromeda Galaxy. Some 3300 emission-line objects have been detected and their velocities measured. Cross-checks against other smaller data sets have confirmed the accuracy of these measurements, and we have also analysed the detected objects in order to separate the PNe from other emission-line objects. Although this paper is primarily intended just to present the data, we can draw a number of intriguing conclusions from even the initial analysis of these observations. Specifically:

- A number of M31’s satellites are detected in the survey, but the existence of Andromeda VIII is brought into question by this larger data set.
- The luminosity function is well reproduced by the usual simple functional form, with no strong evidence for spatial variations that cannot be attributed to modest amounts of obscuration. It has been suggested that the bright end of the luminosity function is dominated by relatively massive stars, so one might expect the PNLF to vary significantly between the spheroid and disk components. The absence of such effects suggests that all PNe in M31 arise from old low-mass stars.
- The number counts of PNe matches that of the R-band photometry, further indicating that both arise from the same old population. With these dynamically-selected number counts of discrete objects, we can also go much deeper than the conventional photometry of M31. There is no evidence for a cut-off in its exponential disk population to beyond four scale-lengths, and there are no signs of a halo population that is distinct from the bulge out to ten effective bulge radii.
- Somewhat unexpectedly, the velocity dispersion of M31 does not drop to zero at large radii, and there is a significant asymmetric drift between the rotational motion and the local circular speed at all radii. These data can be self-consistently reproduced by a simple disk model which is partially supported by random motions even at large radii. If the shape of the velocity ellipsoid remains approximately constant, then M31’s disk must increase in scale-height at large radii or its mass-to-light ratio must increase significantly.
- There is no evidence for any systematic variation in disk PN velocity dispersion with magnitude, again suggesting that PNe of all luminosities arise from a relatively homogeneous old stellar population.

Clearly, this quick pass through the database has only scratched the surface of what can be done with a kinematic survey of this size. We look forward to more detailed dynamical modelling of the full three-dimensional $\{X, Y, v\}$ phase-space data set, as well as tagging the PNe with extra dimensions such as their magnitudes and line ratios. Such analysis will allow us to dig deeper into this rich parameter space in order to further understand the dynamical properties of our nearest large neighbour and its planetary nebula population.

ACKNOWLEDGEMENTS

This research is based on data obtained using the William Herschel Telescope operated by the Isaac Newton Group in La Palma; the support and advice of the ING staff are gratefully acknowledged. We would like to thank Phil Massey and the Local Group Survey team for their assistance. MRM is currently supported by a PPARC Senior fellowship, for which he is most grateful. We would also like

to thank the referee for a timely reading of the paper and a number of helpful suggestions.

REFERENCES

- Bender R., Paquet A., Nieto J.-L., 1991, *A&A*, 246, 349
- Bertin E., Arnouts S., 1996, *A&AS*, 117, 393
- Binney J., Merrifield M., 1998, *Galactic astronomy*. Princeton, NJ : Princeton University Press, 1998.
- Binney J., Tremaine S., 1987, *Galactic dynamics*. Princeton, NJ, Princeton University Press, 1987.
- Braun R., 1991, *ApJ*, 372, 54
- Brinks E., Burton W. B., 1984, *A&A*, 141, 195
- Brinks E., Shane W. W., 1984, *A&AS*, 55, 179
- Cardelli J. A., Clayton G. C., Mathis J. S., 1989, *ApJ*, 345, 245
- Carter D., Sadler E. M., 1990, *MNRAS*, 245, 12P
- Ciardullo R., Durrell P. R., Laychak M. B., Herrmann K. A., Moody K., Jacoby G. H., Feldmeier J. J., 2004, *ApJ*, 614, 167
- Ciardullo R., Feldmeier J. J., Jacoby G. H., Kuzio de Naray R., Laychak M. B., Durrell P. R., 2002, *ApJ*, 577, 31
- Ciardullo R., Jacoby G. H., Ford H. C., Neill J. D., 1989, *ApJ*, 339, 53
- Cox A. N., 2000, *Allen's astrophysical quantities*. Allen's astrophysical quantities, 4th ed. Publisher: New York: AIP Press; Springer, 2000. Edited by Arthur N. Cox. ISBN: 0387987460
- de Jong J. T. A., et al., 2005, *A&A*, 446, 855
- de Vaucouleurs G., 1958, *ApJ*, 128, 465
- de Vaucouleurs G., de Vaucouleurs A., Corwin H. G., Buta R. J., Paturel G., Fouque P., 1991, *Third Reference Catalogue of Bright Galaxies*. Springer-Verlag Berlin Heidelberg New York
- Dehnen W., Binney J. J., 1998, *MNRAS*, 298, 387
- Devereux N. A., Price R., Wells L. A., Duric N., 1994, *AJ*, 108, 1667
- Douglas N. G., et al., 2002, *PASP*, 114, 1234
- Ferguson A. M. N., Gallagher J. S., Wyse R. F. G., 2000, *AJ*, 120, 821
- Ferguson A. M. N., Irwin M. J., Ibata R. A., Lewis G. F., Tanvir N. R., 2002, *AJ*, 124, 1452
- Gerssen J., Kuijken K., Merrifield M. R., 1997, *MNRAS*, 288, 618
- Górny S. K., Stasińska G., 1995, *A&A*, 303, 893
- Halliday C., et al., 2006, Submitted to *MNRAS*
- Huchra J. P., Brodie J. P., Kent S. M., 1991, *ApJ*, 370, 495
- Huchra J. P., Vogeley M. S., Geller M. J., 1999, *ApJS*, 121, 287
- Hui X., Ford H. C., Ciardullo R., Jacoby G. H., 1993, *ApJ*, 414, 463
- Hurley-Keller D., Morrison H. L., Harding P., Jacoby G. H., 2004, *ApJ*, 616, 804
- Ibata R., Chapman S., Ferguson A. M. N., Irwin M., Lewis G., McConnachie A., 2004, *MNRAS*, 351, 117
- Ibata R., Chapman S., Ferguson A. M. N., Lewis G., Irwin M., Tanvir N., 2005, *ApJ*, 634, 287
- Ibata R., Irwin M., Lewis G., Ferguson A. M. N., Tanvir N., 2001, *Nature*, 412, 49
- Irwin M. J., Ferguson A. M. N., Ibata R. A., Lewis G. F., Tanvir N. R., 2005, *ApJL*, 628, L105
- Jacoby G. H., 1989, *ApJ*, 339, 39
- Jacoby G. H., De Marco O., 2002, *AJ*, 123, 269
- Kalirai J. S., Guhathakurta P., Gilbert K. M., Reitzel D. B., Majewski S. R., Rich R. M., Cooper M. C., 2005. arXiv:astro-ph/0512161
- Kent S. M., 1989, *PASP*, 101, 489
- Loinard L., Allen R. J., Lequeux J., 1995, *A&A*, 301, 68
- Magrini L., Corradi R. L. M., Mampaso A., Perinotto M., 2000, *A&A*, 355, 713
- Marigo P., Girardi L., Weiss A., Groenewegen M. A. T., Chiosi C., 2004, *A&A*, 423, 995
- Massey P., Hodge P. W., Holmes S., Jacoby J., King N. L., Olsen K., Smith C., Saha A., 2002, *Bulletin of the American Astronomical Society*, 34, 1272
- Mateo M. L., 1998, *ARA&A*, 36, 435
- McConnachie A. W., Irwin M. J., Ferguson A. M. N., Ibata R. A., Lewis G. F., Tanvir N., 2005, *MNRAS*, 356, 979
- McConnachie A. W., Irwin M. J., Ibata R. A., Ferguson A. M. N., Lewis G. F., Tanvir N., 2003, *MNRAS*, 343, 1335
- McElroy D. B., 1983, *ApJ*, 270, 485
- Merrett H. R., et al., 2003, *MNRAS*, 346, L62
- Meyssonnier N., Lequeux J., Azzopardi M., 1993, *A&AS*, 102, 251
- Monet D. G., et al., 2003, *AJ*, 125, 984
- Morrison H. L., Harding P., Hurley-Keller D., Jacoby G., 2003, *ApJL*, 596, L183
- Narayan C. A., Jog C. J., 2002, *A&A*, 390, L35
- Nolthenius R. A., Ford H. C., 1984, *BAAS*, 16, 456
- Oke J. B., 1974, *ApJS*, 27, 21
- Oke J. B., 1990, *AJ*, 99, 1621
- Oke J. B., Gunn J. E., 1983, *ApJ*, 266, 713
- Peimbert M., 1990, *Revista Mexicana de Astronomia y Astrofisica*, 20, 119
- Reitzel D. B., Guhathakurta P., 2002, *AJ*, 124, 234
- Sambhus N., Gerhard O., Méndez R. H., 2006, *AJ*, 131, 837
- Schlegel D. J., Finkbeiner D. P., Davis M., 1998, *ApJ*, 500, 525
- Sevenster M. N., Chapman J. M., Habing H. J., Killeen N. E. B., Lindqvist M., 1997, *A&AS*, 122, 79
- Simien F., Prugniel P., 2002, *A&A*, 384, 371
- van Dokkum P. G., 2001, *PASP*, 113, 1420
- Walterbos R. A. M., Kennicutt R. C., 1987, *A&AS*, 69, 311
- Walterbos R. A. M., Kennicutt R. C., 1988, *A&A*, 198, 61